




Article

Hydrodeoxygenation of Phenolic Compounds and Lignin Bio-Oil Surrogate Mixture over Ni/BEA Zeolite Catalyst and Investigation of Its Deactivation

Antigoni G. Margellou ^{1,*}, Foteini F. Zormpa ¹, Dimitrios Karfaridis ², Stamatia A. Karakoulia ³ and Konstantinos S. Triantafyllidis ^{1,4,5,*}

¹ Department of Chemistry, Aristotle University of Thessaloniki, 54124 Thessaloniki, Greece

² Department of Physics, Aristotle University of Thessaloniki, 54124 Thessaloniki, Greece; dkarfari@physics.auth.gr

³ Chemical Process and Energy Resources Institute, Centre for Research and Technology Hellas, 57001 Thessaloniki, Greece; matoula@certh.gr

⁴ Department of Chemistry, King Fahd University of Petroleum and Minerals, Dhahran 31261, Saudi Arabia

⁵ Interdisciplinary Research Center for Refining and Advanced Chemicals, King Fahd University of Petroleum & Minerals, Dhahran 31261, Saudi Arabia

* Correspondence: amargel@chem.auth.gr (A.G.M.);

ktrianta@chem.auth.gr or k.triantafyllidis@kfupm.edu.sa (K.S.T.)

+ ^{4,5} are primary affiliations of. K.S.T.

Abstract: Lignin is one of the main structural components of lignocellulosic biomass and can be utilized to produce phenolic compounds that can be converted downstream to cycloalkanes and aromatics, which are useful as drop-in road or aviation biofuels. Within this study, the hydrodeoxygenation of model phenolic/aromatic compounds and surrogate mixture simulating the light fraction of lignin fast-pyrolysis bio-oil was performed under mild reaction conditions. Ni/BEA zeolite was selected as a catalyst to investigate the conversion and the product selectivity of alkyl phenols (phenol, catechol, cresols), methoxy-phenols (guaiacol, syringol, creosol), aromatics (anisole, 1,2,3-trimethoxybenzene) and dimer (2-phenoxy-1-phenyl ethanol) compounds towards (alkyl)cycloalkanes. The hydrodeoxygenation of a surrogate mixture of eleven phenolic and aromatic compounds was then studied by investigating the effect of reaction conditions (temperature, time, H₂ pressure, surrogate mixture concentration, and catalyst-to-feed ratio). The conversion of model compounds was in the range of 80–100%, towards a 37–81% (alkyl)cycloalkane yield, being strongly dependent on the complexity/side-chain group of the phenolic/aromatic ring. Regarding the hydrodeoxygenation of the surrogate mixture, 59–100% conversion was achieved, with up to a 72% yield of C₆–C₉ cycloalkanes. Characterization of spent catalysts showed that the hydrodeoxygenation of surrogate mixture led to carbonaceous depositions on the catalyst, which can be limited under lower temperatures and longer reaction conditions, while after regeneration, the physicochemical properties of catalysts can be partially recovered.

Keywords: lignin fast-pyrolysis bio-oil; surrogate mixture; phenolic compounds; hydrodeoxygenation; cycloalkanes; sustainable aviation and road fuels; Ni/BEA zeolite; deactivation



Academic Editor: Mohammad Mozahar Hossain

Received: 16 December 2024

Revised: 31 December 2024

Accepted: 4 January 2025

Published: 7 January 2025

Citation: Margellou, A.G.; Zormpa, F.F.; Karfaridis, D.; Karakoulia, S.A.; Triantafyllidis, K.S. Hydrodeoxygenation of Phenolic Compounds and Lignin Bio-Oil Surrogate Mixture over Ni/BEA Zeolite Catalyst and Investigation of Its Deactivation.

Catalysts **2025**, *15*, 48. <https://doi.org/10.3390/catal15010048>

Copyright: © 2025 by the authors.

Licensee MDPI, Basel, Switzerland.

This article is an open access article distributed under the terms and conditions of the Creative Commons Attribution (CC BY) license

(<https://creativecommons.org/licenses/by/4.0/>).

1. Introduction

Nowadays, aviation companies as well as public organizations have enacted new directives for replacing (at least partially) conventional, petroleum-based aviation fuels with

sustainable aviation fuels (SAFs) originating mainly from biomass. According to the European Commission's directive, SAFs should be blended with kerosene-type fuels at 2% in the final fuel mix during 2025, with the percentage gradually increasing to 70% by 2050 [1]. Aviation fuels are typically composed of normal and iso-paraffinic C₈–C₁₆ hydrocarbons, while aromatic hydrocarbons and cycloparaffins also exist in lower amounts. Till now, the most promising feedstocks for the production of bio-renewable aviation fuels are lipids derived from vegetables, animal fats, and microalgae enriched in fatty acids and triglycerides. After suitable extraction processes, lipids can be converted to C₈–C₁₆ hydrocarbons via hydrotreatment and utilized as jet fuel or green diesel fuel [2–5]. Apart from lipids, lignocellulosic biomass can be utilized to produce bio-based aviation fuels. Carbohydrates of lignocellulosic biomass (cellulose and hemicellulose) can provide linear and branched paraffinic hydrocarbons, while lignin can be converted to aromatics and cycloalkanes [6]. Sugars can be converted to C₈–C₁₅ hydrocarbons via cascade hydrolysis/dehydration, condensation/coupling, and hydrodeoxygenation reactions [7–11].

Focusing on lignin, the production of aviation fuels requires two steps: the initial depolymerization of lignin to phenolic/aromatic bio-oils, and the subsequent hydrodeoxygenation of bio-oils to cycloalkanes and aromatics. The depolymerization of lignin is usually carried out via thermocatalytic processes, such as fast pyrolysis and hydrogenolysis to produce phenolic/aromatic bio-oils with high oxygen content, which results in poor quality and stability [12–17]. Although catalytic fast pyrolysis can substantially decrease the oxygen content of lignin bio-oils, downstream catalytic hydrotreatment/hydrodeoxygenation is required to enhance deoxygenation along with aromatic ring saturation depending on catalyst and process conditions [18,19]. The complex nature of lignin bio-oils hinders the effective conversion of bio-oils to hydrocarbons, and thus fundamental research has been carried out utilizing model compounds. A wide variety of alkoxy- and alkyl-phenolic/aromatic compounds have been utilized as model compounds, including phenol, guaiacol, syringol, cresols, catechol, anisole, vanillin, etc. containing at least one O-H, C-O-C, or C-C bond [20–28]. Apart from phenolic/aromatic monomers, dimers simulating the most abundant interunit linkage of lignin (β -O-4, β - β , β -5, etc.) have also been used [25,29–34]. Hydrodeoxygenation studies of real lignin bio-oil fractions have been rarely reported. More frequently, whole-biomass pyrolysis bio-oils have been used and studied for the production of cycloalkanes and aromatics [21,35–37].

The hydrodeoxygenation efficiency and selectivity of the products are strongly dependent on the catalyst properties. Classic hydrotreatment catalysts based on NiMo supported by Al₂O₃ are widely utilized in the hydrodeoxygenation of phenolic compounds but mainly lead to the formation of intermediates rather than complete deoxygenated products [38,39]. Aiming to overcome the main drawbacks of those catalysts, such as the low deoxygenation efficiency, the coke formation tendency, and the continuous need for sulfidation along with the higher hydrogen pressure required, bifunctional catalysts have been developed for the hydrodeoxygenation of phenolic compounds [40,41]. Bifunctional catalysts are based on noble or transition metals supported mainly by acidic aluminosilicates, i.e., zeolites, silica-alumina, etc., combining both Brønsted and Lewis acid sites [42]. Regarding the metal, noble metals, such as Pt, Ru, and Pd, and transition metals, such as Ni, Fe, and Co, are widely used in the hydrodeoxygenation of phenolic compounds, but nickel has been recognized as a cheap, abundant, and effective metal for this reaction/process [43–45]. Furthermore, a wide variety of metal oxides, such as TiO₂ and ZrO₂, have also been used as supports in the hydrodeoxygenation of model compounds and real biomass pyrolysis bio-oil [21]. It has been shown that the physicochemical characteristics of the supports and metal-support interactions may have a significant impact on the reaction pathway and product selectivity [46–48]. Zeolites, being amongst the most studied materials as

supports for the hydrodeoxygenation of phenolics and real bio-oils, are crystalline aluminosilicates with different structures and micro/mesoporous and acidic properties that exhibit good stability and the ability to control product selectivity. Zeolite-based catalysts have been used in the hydrodeoxygenation of real bio-oils and a wide range of phenolic compounds with different side groups [18,20,29,34,49–53]. Tailoring of acid site content and strength, as well as the structure/size of micro/mesopores, may minimize coke formation and steric hindrance phenomena, leading to enhanced conversion and selectivity of the targeted cycloalkanes [20,34,49].

The aim of this work is the optimization of the hydrodeoxygenation of a surrogate mixture simulating the light fraction of lignin fast-pyrolysis bio-oil. Based on previous studies [20,49,54], a Ni/BEA catalyst was selected as the optimum catalyst for hydrodeoxygenation under relatively mild reaction conditions in terms of temperature, H₂ pressure, time, and minimizing steric hindrance. Prior to the surrogate mixture, different phenolic and aromatic model compounds were used to study the effect of the phenyl side group in the hydrodeoxygenation and the selectivity of the products. The hydrodeoxygenation of the surrogate mixture was performed at a high concentration (50% *w/v*) compared to the literature (4–20% *w/v*) to investigate the potential of an up-scale commercial process. Furthermore, in this study, the deactivation of catalysts due to carbonaceous species was studied, as well as the characterization of regenerated catalysts, to examine their stability.

2. Results

2.1. Catalyst Characterization

The crystalline structure of the catalyst was determined via XRD analysis and as can be observed in Figure S1a, the reduced catalyst exhibits the metallic phase of nickel (Ni⁰), as can be confirmed by the diffraction peaks at $2\theta = 44.5, 51.9, \text{ and } 76.4^\circ$, while the rest of the peaks revealed that the structure of beta zeolite (BEA) is preserved in the final catalyst. The crystallite size, determined via the Scherrer equation, is equal to 14 nm. Regarding the porous properties, the catalyst exhibits a combination of Type I and Type IV isotherms with an H4 hysteresis loop (Figure S1b), corresponding to microporous materials with enhanced meso/macroporous characteristics, according to the IUPAC classification [55]. The specific surface area calculated via the BET equation is equal to 562 m²/g, and the total pore volume calculated at $P/P_0 = 0.99$ is estimated at 1.151 cm³/g. These values are slightly lower compared to those of the parent BEA zeolite, which yields $S_{\text{BET}} = 596 \text{ m}^2/\text{g}$ and $V_{\text{tot}} = 1.263 \text{ cm}^3/\text{g}$. The microporous area and volume of the Ni/BEA catalyst were calculated via t-plot analysis and are equal to 371 m²/g and 0.154 cm³/g, respectively. The relevant values of the parent zeolite were $S_{\text{micro}} = 376 \text{ m}^2/\text{g}$ and $V_{\text{micro}} = 0.153 \text{ cm}^3/\text{g}$, proving that the metal loading of 10 wt.% does not affect the microporous characteristics of BEA zeolite. The same conclusions can be drawn from the BJH pore-size distributions. The average pore diameter of the 10%Ni/BEA catalyst is 80 Å, slightly lower than that of the parent zeolite (85 Å). Furthermore, the catalyst exhibits both Brønsted and Lewis acid sites. The number of total acid sites is 284 μmol/g, with 182 μmol/g corresponding to Lewis acid sites and 102 μmol/g to Brønsted acid sites. When compared to the parent BEA zeolite, it can be seen that the addition of nickel led to a decrease in Brønsted acid sites from 180 μmol/g to 102 μmol/g and a decrease in Lewis acid sites from 320 to 182 μmol/g, mainly due to catalyst workup (impregnation, drying, calcination, reduction).

2.2. Model Compound Hydrodeoxygenation

The hydrodeoxygenation of model compounds was performed at 220 °C, 1 h, 50 bar H₂, and C/F = 0.2. The reaction conditions were selected according to the optimization

study carried out in our previous work [20]. The compounds used in this study were grouped into four main categories:

- i. Hydroxy- and methyl-substituted phenols (phenol, o-/m-cresol, and catechol) with C-O-H and C-C side chains on the phenolic ring.
- ii. Alkoxy (methoxy)-substituted phenols (guaiacol, syringol, 2-methoxy-4-methyl-phenol) with at least one C-O-C side chain,
- iii. Alkoxy (methoxy-) substituted aromatics (anisole and 1,2,3-trimethoxybenzene) with one and three C-O-C side chains.
- iv. Dimer (2-phenoxy-1-phenyl ethanol) is used as a model compound to simulate the small oligomers of lignin fast-pyrolysis bio-oil.

Regarding the first category, i.e., the hydroxy- and methyl-substituted phenols, the hydrodeoxygenation led to the complete conversion of all compounds, while differences were observed in the selectivity of the products (Figure 1). The conversion of the simplest phenolic compound (phenol) led to the formation of cyclohexane (43% yield), and methyl-cyclopentane (9.5%) formed via the isomerization of cyclohexane. The addition of a second hydroxyl group in the ortho position in catechol did not influence the conversion but slightly decreased the yield of cyclohexane to 34.7% and increased the yield of methyl-cyclopentane to 13.4%. Furthermore, based on the GC-MS analysis (Figure S2), methyl-cyclohexane, 1,1-bicyclohexyl, and (cyclopentylmethyl)cyclohexane were also identified in lower amounts. The lower cyclohexane yield is attributed to the different adsorption mechanism of catechol compared to phenol due to the addition of the second hydroxyl group [50]. The lower reactivity of catechol was also observed for other catalytic systems, such as nickel phosphides [56]. On the other hand, the addition of a methyl group in the ortho or meta positions shifted the selectivity towards methyl-cyclohexane, proving that the mild hydrodeoxygenation conditions did not induce cleavage of C-C bonds and thus maintained the carbon number of the reactant phenolics. The addition of the methyl group in the o- position led to a 77.5% yield of methyl-cyclohexane, while the addition of the methyl group in the m- position led to slightly lower yields of 62.2% and 7.4% methyl-cyclopentane. Compared to cyclohexane, methyl-cyclohexane produced via the hydrodeoxygenation of cresols shows a higher isomerization tendency towards alkyl-cyclopentanes, as can be observed in the GC-MS analysis (Figure S2).

The second group of model compounds studied was the one with alkoxy-phenolic and aromatic compounds. The addition of a methoxy group in the ortho position of the phenolic ring (guaiacol) did not have any effect on conversion and cyclohexane yield. Guaiacol was fully converted to cyclohexane (46.5% yield) and methyl-cyclopentane (11.6% yield) (Figure 2). Furthermore, the hydrodeoxygenation of guaiacol led to the formation of the aromatic dimers 1,1-bicyclohexyl and (cyclopentylmethyl)cyclohexane at lower relative concentrations of 1.2% and 2.1%, respectively (Figure S3). Another oxygenated phenolic compound frequently identified in lignin fast-pyrolysis bio-oils is 2-methoxy-4-methyl phenol. The hydrodeoxygenation using the Ni/BEA catalyst led to the full conversion of 2-methoxy-4-methyl phenol towards 59.4% methyl-cyclohexane, 10.6% ethyl-cyclohexane, and 11.0% methyl-cyclopentane. Previous works have shown that Ni/BEA catalysts exhibit higher activity compared to other catalysts using zeolites or other supports at relatively mild reaction conditions [53,54,57]. More specifically, mixtures of carbon with zeolites used as supports for palladium-based catalysts did not facilitate the complete hydrodeoxygenation of guaiacol and led mainly to the formation of phenol and cyclohexanone [53]. Regarding nickel-based catalysts, Ni/BEA exhibited a high yield of complete deoxygenated compounds (58%), which was further increased to 76% under more intense conditions (300 °C, 3.5 h, 15 wt.% Ni) [54]. Furthermore, the bifunctional Ni/BEA catalyst exhibited higher conversion and cyclohexane yields than the classic NiMo hydrotreatment catalyst,

which led to lower conversion (18%) and 80% cyclohexane selectivity at a higher reaction temperature (350 °C) [58].

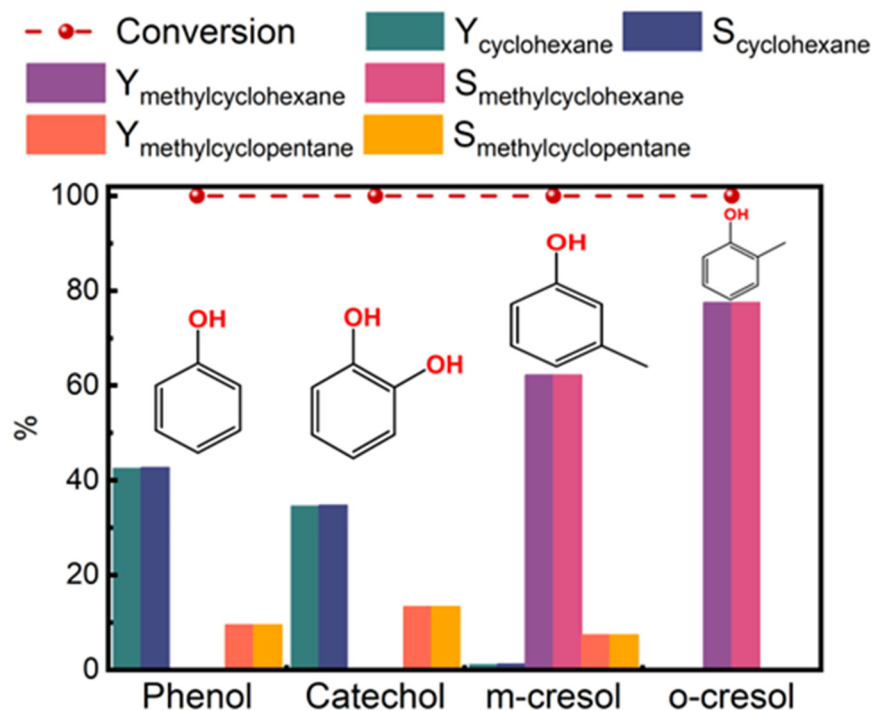


Figure 1. Hydrodeoxygenation of hydroxy and alkyl-substituted phenols at 220 °C, 1 h, 50 bar H₂, 10% Ni/BETA (12.5), C/F = 0.2.

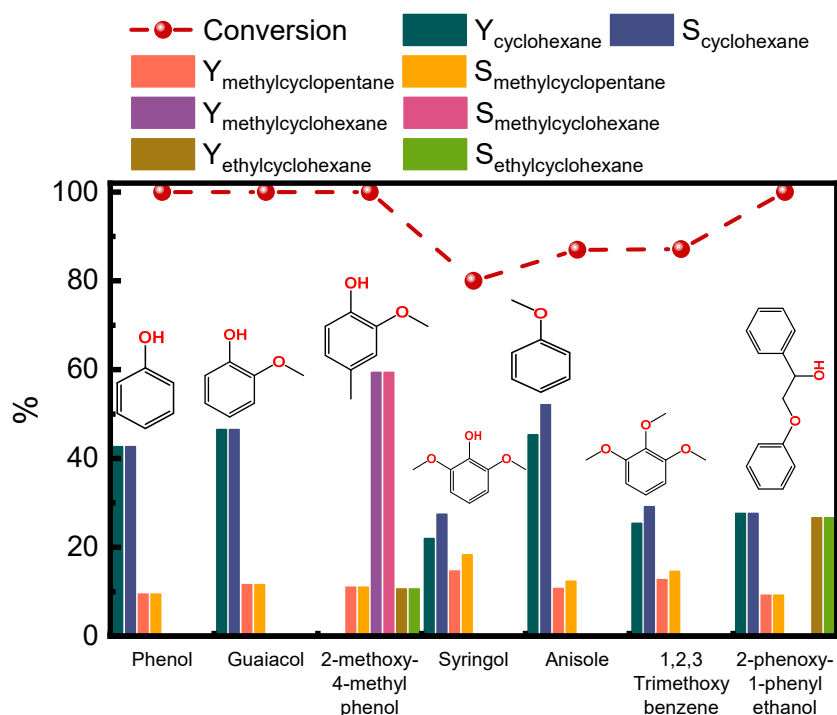


Figure 2. Hydrodeoxygenation of alkoxy phenols/benzene and dimer at 220 °C, 1 h, 50 bar H₂, 10% Ni/BETA (12.5), C/F = 0.2.

The results of the present study indicate that Ni/BEA catalyzed the cleavage of C_{AR}-OH and C_{AR}-OCH₃ bonds while retaining the C_{AR}-CH₃ bonds in the various model compounds tested. Additionally, the acid sites of the zeolite support favored the isomerization of methyl-cyclohexane to many dimethyl-cyclopentanes and ethyl-cyclopentane, as

can be observed in the GC-MS analysis in Figure S3. On the other hand, the addition of the second methoxy group (i.e. syringol) led to lower conversion (80%) and a significantly lower cyclohexane yield (22%). The reason for the lower conversion of syringol compared to guaiacol and the hydroxy/alkylated-substituted phenolic compounds is the steric hindrance caused by the zeolite micropores. The structure of beta zeolite is three-dimensional, containing 12×12 ring channels with sizes $6.4 \text{ \AA} \times 7.6 \text{ \AA}$ and $5.6 \text{ \AA} \times 5.6 \text{ \AA}$ [59]. The maximum width of the syringol molecule is around 8.92 \AA , as shown in the calculations in Figure S4 performed via Jmol [60]. Consequently, syringol cannot easily enter the pores of zeolite BEA, in contrast to phenol, catechol, cresols, and guaiacol, which exhibit maximum widths in the range of $5.61\text{--}7.15 \text{ \AA}$ (Figure S4). Similar observations have been observed for other catalytic processes involving zeolites with specific pore sizes/shapes and bulky reactant molecules [49,61].

Regarding the methoxy-aromatics, i.e., anisole and 1,2,3-trimethoxybenzene, the replacement of the hydroxyl group (in phenol) by a methoxy group led to lower conversion of anisole (87%) but similar cyclohexane (45.3%) and methyl-cyclopentane (10.7%) yields compared to those obtained with phenol. Anisole can be converted to phenol and cresol via transalkylation on the Brønsted acid sites of beta zeolite, and then cresol is hydrodeoxygenated to methyl-cyclohexane [62,63]. This reaction pathway was confirmed via GC-MS analysis, where methyl-cyclohexane was identified at a very low relative concentration (2.23%). Compared to previous works, the Ni/BEA catalyst of the present study exhibited higher catalytic activity than other Ni/BEAs, which exhibited only 18.8% anisole conversion and a 7.5% yield of cyclohexane, or compared to nickel catalysts supported by natural zeolites, which showed 28.9–33.6% conversion and a 17.8–16.6% cyclohexane yield at $230 \text{ }^\circ\text{C}$ [62]. Furthermore, Ni/BEA exhibited a higher cyclohexane yield than Re-MoO_x/TiO₂, which showed lower conversion (40%) and higher selectivity towards aromatic hydrocarbons [64]. Further addition of methoxy groups in the benzyl ring (i.e., 1,2,3-trimethoxy benzene) led to similar conversion (87%) but a significantly lower cyclohexane yield (25.4%). The lower yield of cyclohexane is attributed to steric hindrance effects, which only allowed the partial conversion of bulk 1,2,3-trimethoxy benzene with a maximum width of 8.92 \AA (Figure S4).

The dimer 2-phenoxy-1-phenyl ethanol was used as a model compound to simulate the β -O-4 interunit linkages existing in the phenolic oligomers of lignin bio-oil. As can be observed in Figure 2, the hydrodeoxygenation under mild reaction conditions led to the complete conversion of the compound to 27.7% cyclohexane, 26.7% ethyl-cyclohexane, and 9.2% methyl-cyclopentane. The rest of the compounds were identified via GC-MS analysis (Figure S3) and were mainly alkyl-substituted cyclohexanes and cyclopentanes. It can be highlighted that despite the higher length (11.75 \AA) of the compound, the compound can enter into the zeolite pore with one of the two aromatic rings, which have a maximum width of 4.97 \AA , and thus the effect of steric hindrance is minimized. The results from the hydrodeoxygenation of the dimer proved that the nickel-based bifunctional catalysts are active in catalyzing mainly the C-O linkages and maintaining the C-C bonds, while their activity can be compared to that of the noble-metal-based catalysts described in the literature [25,31,65]. Based on the GC-MS analysis, as well as on literature data, the proposed hydrodeoxygenation pathways of 2-phenoxy-1-phenyl ethanol are shown in Figure 3. In the first step, cleavage of the β -O-4 ether bond takes place via hydrogenolysis to 1-phenylethan-1-ol and anisole. These compounds were not identified in the GC-MS analysis, but they were both assumed based on the complete hydrogenated products and similar literature results [66–68]. 1-phenylethan-1-ol is converted to ethylbenzene via dehydration, which is further converted to ethyl-cyclohexane via aromatic ring hydrogenation with 1-ethyl-cyclohexene as the intermediate. Then, the ethyl-cyclohexane is isomerized to

1,3-dimethyl-cyclohexane and 1-ethyl-3-methyl-cyclopentane on zeolitic acid sites. Then, phenol is converted to cyclohexane via cyclohexanol dehydration, which further isomerizes to methyl-cyclopentane, with both steps being catalyzed by zeolite acid sites. On the other hand, the hydrogenolysis of 2-phenoxy-1-phenyl ethanol can lead to the formation of 2-phenylacetaldehyde, which provides toluene via decarbonylation on Lewis acid sites of beta zeolite [69]. Toluene can be further hydrogenated to methyl-cyclohexane. Carbon-carbon coupling reactions may lead to the formation of 1,1'-methylenebis cyclohexane dimer, while the reaction between ethyl-cyclohexane and toluene leads to the formation of 2-cyclohexylethyl-benzene. The compounds of the final product mixture were within the carbon number distribution range of C₆–C₁₃. In comparison with literature data, the Ni/BEA of this study exhibited higher catalytic activity than Cu_xNi_y/MgO catalysts, which led to 88.6%mol ethylbenzene and oxygenated intermediates at 150 °C and 5 h [66], and Ni_xCo_yAl, which exhibited the same product distribution (95.9% yield of ethylbenzene) under similar reaction conditions (180 °C, 2 h) [67]. Furthermore, nickel enhanced the complete hydrodeoxygenation of dimer compared to pure (metal-free) zeolites (HY, BETA, ZMS-5), which resulted in the formation of phenol and oxygenated aromatics at 240 °C and 1 h using ethanol as a hydrogen donor solvent [68].

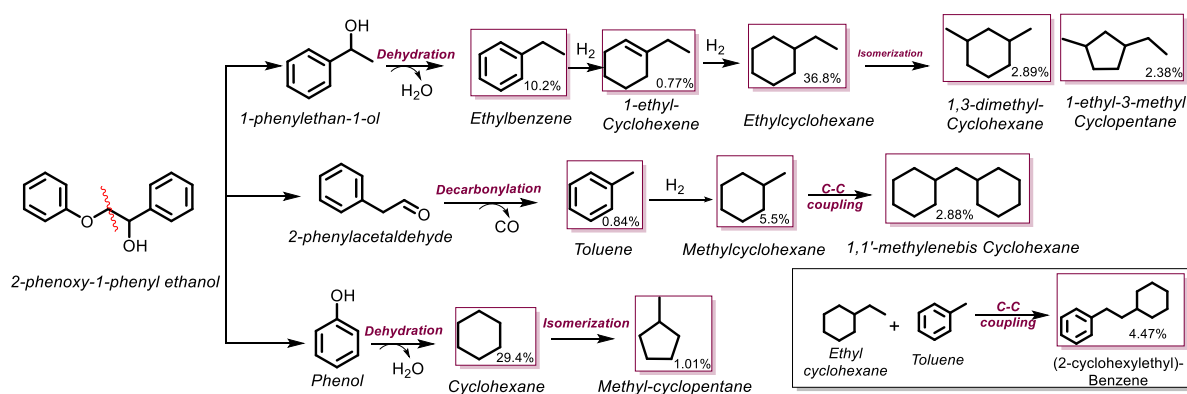


Figure 3. Proposed hydrodeoxygenation pathways of 2-phenoxy-1-phenyl ethanol. Compounds in red frames were identified via GC-MS analysis; the red wave line in the reactant compound indicates the main linkage cleaved during hydrodeoxygenation.

2.3. Hydrodeoxygenation of Surrogate Mixture

The hydrodeoxygenation of the surrogate mixture was thoroughly studied under different reaction conditions, such as temperature, hydrogen pressure, time, catalyst-to-feed ratio (C/F), surrogate mixture concentration, and stirring rate.

Under the basic reaction conditions, i.e., using 50% *w/v* surrogate mixture in *n*-hexadecane at 220 °C, 1 h, initial H₂ pressure of 50 bar, 400 rpm, and C/F = 0.2, it was shown that hydrogen is consumed, leading to high conversion (91%) of the surrogate mixture but quite a low total non-oxygenated compound yield (9.2%) and, more specifically, 1.6% cyclohexane, 2.9% methyl-cyclohexane, 0.9% ethyl-cyclohexane, and 1.1% methyl-cyclopentane (Figure 4). According to the GC-MS analysis, the composition of the final mixture had 45.6% alkyl-cycloalkanes, 2.4% aromatics, and 51.9% non-converted phenolic/aromatic compounds, as can be observed in Figure 5. When the hydrogen pressure was kept steady by continuous feeding of external hydrogen, a similar conversion level was obtained (90%), but this time the hydrogenation reactions were enhanced, and product yield and distribution were substantially affected. The total non-oxygenated compounds quantified by GC-FID remarkably increased to 29%, and the most abundant compounds were 7.8% cyclohexane, 14.6% methyl-cyclohexane, 1.2% ethyl-cyclohexane, and 1.9% methyl-cyclopentane. The higher concentration of non-oxygenated

compounds was also confirmed via GC-MS analysis, and the final product was composed of 58.9% alkyl-cycloalkanes and 1.8% aromatics, while the unconverted phenolic/aromatic compounds were 33.3%. Furthermore, few alkyl-phenols/cyclohexanones and oxygenated aromatics were identified (~6%) as intermediates due to partial hydrodeoxygenation efficiency (Figure 5). Further increase of the (initial) hydrogen pressure to 70 bar increased the total non-oxygenated compounds to 37.7%, with 13.2% cyclohexane, 24.8% methyl-cyclohexane, 1.0% ethyl-cyclohexane, and 2.4% methyl-cyclopentane. The higher hydrogen availability enhanced the hydrogenation of intermediates to complete saturated compounds, resulting in 54.8% alkyl-cycloalkane with lower aromatic products (0.7%), according to the GC-MS analysis. The hydrogen pressure also slightly influenced the carbon number distribution of the products, as can be observed in Figure 6. The products contained C₅–C₉ compounds, while C₁₁–C₁₃ compounds, such as 1,1-bicyclohexyl or (cyclopentylmethyl)-cyclohexane, were also formed due to hydroalkylation and C–C coupling reactions. By increasing the hydrogen pressure from 50 to 70 bar, the relative concentration of C₆–C₇ compounds slightly decreased, while the concentration of C₈–C₉ compounds increased. Compared to the feedstock's carbon number distribution (C₆–C₁₀), the mild hydrodeoxygenation conditions slightly shifted the carbon number distribution to C₅–C₉ due to demethylation (removal of CH₄) and decarboxylation (removal of CO₂) reactions, in accordance with the gaseous product analysis shown in Figure S4.

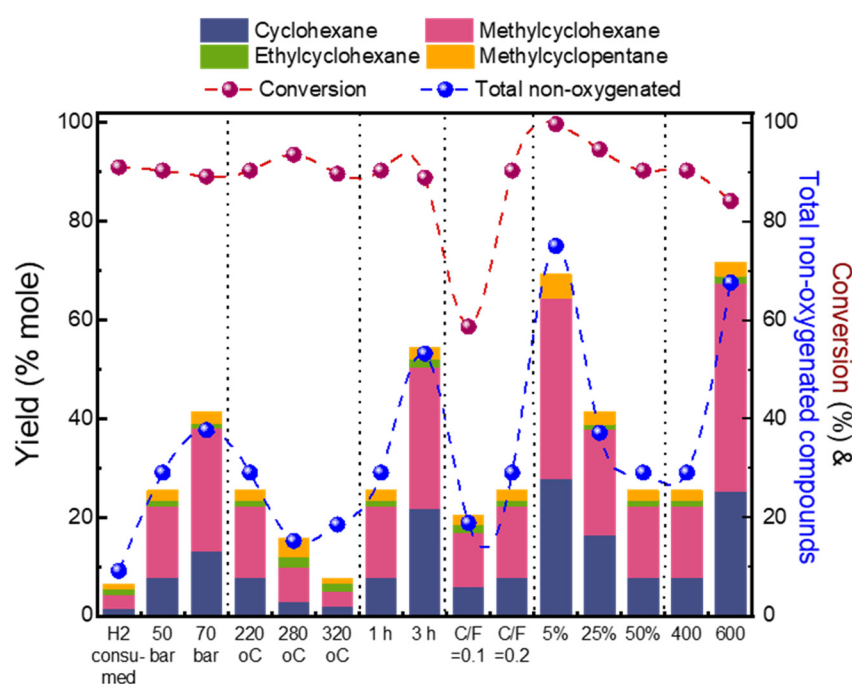


Figure 4. Effect of different reaction conditions on the hydrodeoxygenation of the surrogate mixture over 10%Ni/BETA (12.5). The basic conditions were: 220 °C, 1 h, 50 bar H₂, 50 wt.% surrogate in hexadecane, C/F = 0.2, stirring rate = 400 rpm.

The most profound effect on the hydrodeoxygenation of the surrogate mixture was caused by the changes in the reaction temperature. The effect of reaction temperature was studied in the range of 220–320 °C using 50% *w/v* surrogate mixture in n-hexadecane, 50 bar H₂, 1 h, 400 rpm, and C/F = 0.2. The gradual increase in the reaction temperature did not significantly influence the conversion of the surrogate mixture (89–93%) but mainly affected the product distribution. An increase in the reaction temperature from 220 to 280 °C led to lower non-oxygenated compounds (from 30% to 15%), with the most abundant compounds being 3.1% cyclohexane, 6.9% methyl-cyclohexane, 2.1% ethyl-cyclohexane, and 3.6% methyl-cyclopentane (Figure 4). A further increase to 320 °C led to even less cy-

cloalkanes, with 1.9% cyclohexane, 3.0% methyl-cyclohexane, 1.8% ethyl-cyclohexane, and 0.7% methyl-cyclopentane. Based on the GC-MS analysis results (Figure 5), it is observed that the increase in the reaction temperature enhanced the conversion of the phenolic and aromatic reactant (feed) compounds of the surrogate mixture, whose concentration was decreased to 14.7% at 320 °C. Nevertheless, the cycloalkanes concentration in the products decreased from 58.8% at 220 °C to 27.7% at 320 °C. The GC-MS analysis data actually showed that the higher reaction temperatures enhanced the selectivity towards aromatics products, whose concentration progressively increased from 1.8% at 220 °C to 10.8% at 320 °C, as well as towards phenolic (mainly alkylphenols) and aromatic oxy-intermediates, whose concentrations increased to 42.3%. These results can be justified on the basis of the observed (discussed below) increased coke formation on the catalyst as the reaction temperature increased. It is thus clear that a balance between relatively low reaction temperatures and sufficient hydrogenation reactivity is the key to efficient hydrodeoxygenation of such types of light lignin bio-oil surrogates.

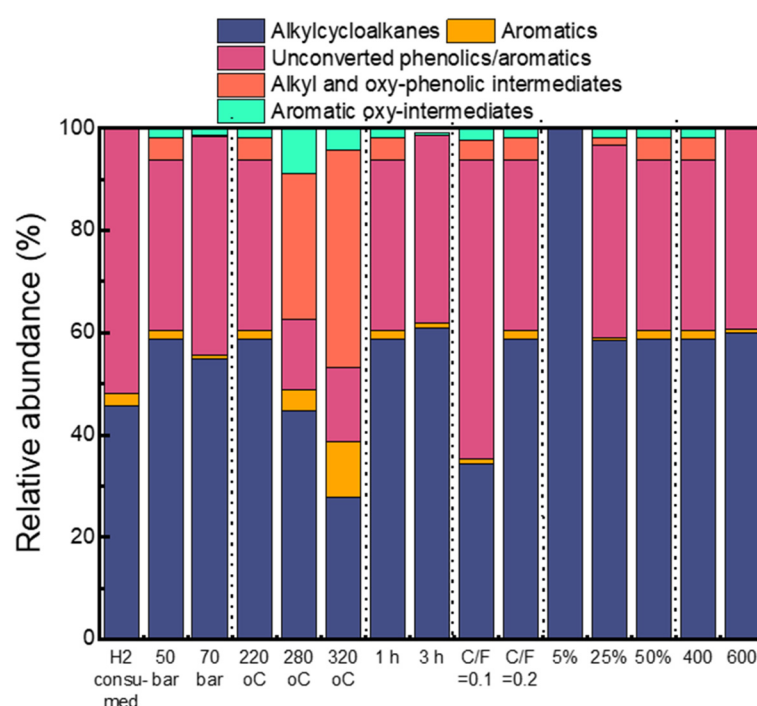


Figure 5. Effect of different reaction conditions on the product distribution of surrogate mixture hydrodeoxygenation over 10%Ni/BETA (12.5). The basic conditions were: 220 °C, 1 h, 50 bar H₂, 50 wt.% surrogate in hexadecane, C/F = 0.2, stirring rate = 400 rpm.

Apart from the product composition, the reaction temperature significantly influenced the carbon number distribution. The gradual increase in the reaction temperature shifted the carbon number distribution to higher-molecular-weight alkyl-cycloalkanes (C₈–C₁₁), as shown in Figure 6, due to hydroalkylation reactions decreasing the C₅–C₆ compounds.

The prolonged reaction time (3 h) also enhanced the formation of alkyl-cycloalkanes (Figure 4). The total non-oxygenated compounds increased from 29% (1 h) to 53% (3 h), with the concentration of the most abundant compounds being 21.9% cyclohexane, 28.7% methyl-cyclohexane, 1.5% ethyl-cyclohexane, and 2.4% methyl-cyclopentane. The beneficial effect of the prolonged reaction time in the hydrodeoxygenation of various phenolic monomers has also been shown in previous works [20,70,71]. Furthermore, the higher reaction time enhanced the formation of C₈–C₉ cycloalkanes instead of C₇ cycloalkanes, as shown in the carbon number distribution of Figure 6, while it also favored the formation of CO₂ in gaseous products due to enhanced decarboxylation (Figure S5).

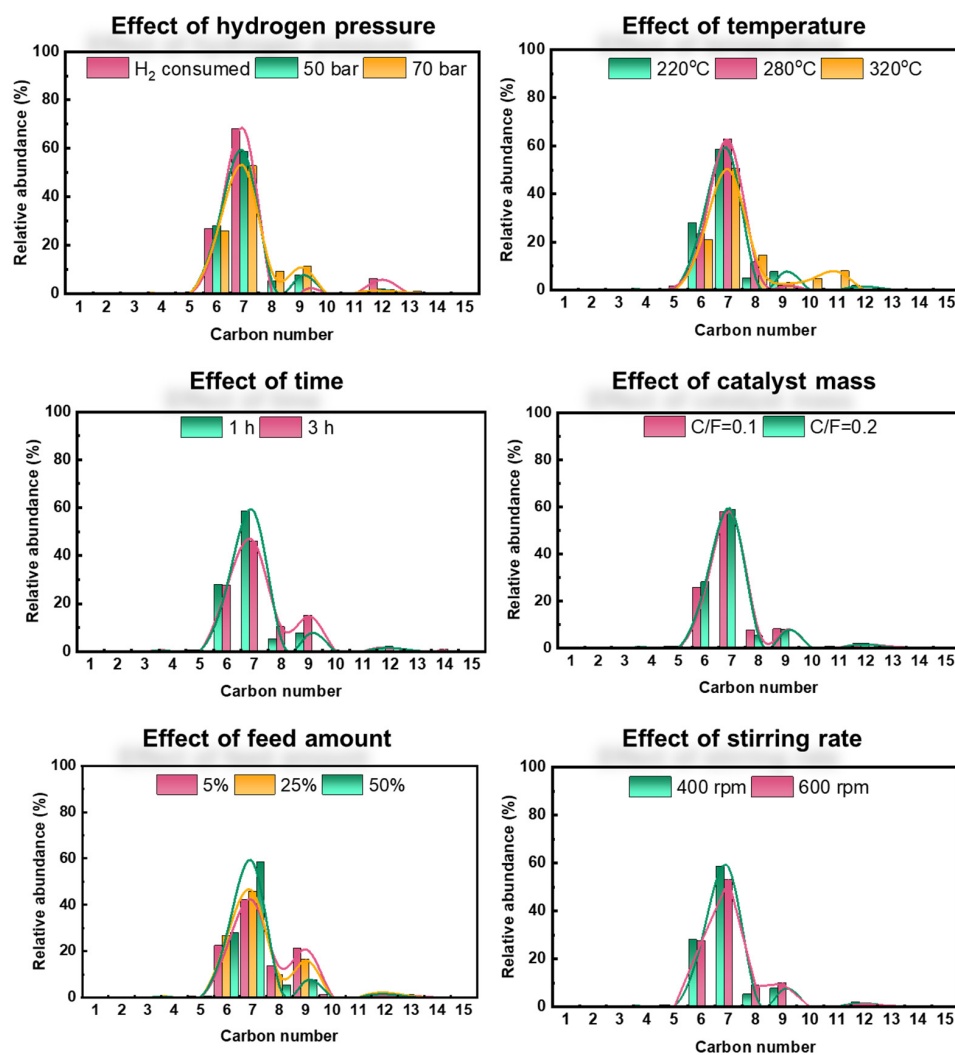


Figure 6. Effect of different reaction conditions on carbon number distributions of non-oxygenated compounds identified in the hydrodeoxygenation of the surrogate mixture over 10%Ni/BETA (12.5).

Regarding the catalyst mass, two different catalyst-to-feed ratios were tested at 50% *w/v* surrogate mixture in *n*-hexadecane, 220 °C, 1 h, 50 bar H₂, and 400 rpm: C/F = 0.1 and C/F = 0.2. At the lower ratio of C/F = 0.1, the conversion of the surrogate mixture was substantially lower (59%) than the conversion using C/F = 0.2 (92%) due to the fewer available active sites. The lower conversion led to a relatively low yield of total non-oxygenated compounds (18.9%), with 5.9% cyclohexane, 11.1% methyl-cyclohexane, 1.5% ethyl-cyclohexane, and 2.0% methyl-cyclopentane. Still, the yield of non-oxygenated compounds at C/F = 2 was not increased substantially despite the profound increase in conversion (Figure 4).

In order to clarify the reason for the low yields of cycloalkanes, two different approaches were followed. In the first approach, the effect of the surrogate mixture concentration (i.e., 5, 25, and 50% *w/v* in hexadecane) was studied at 220 °C, 1 h, 50 bar H₂, 400 rpm, and C/F = 0.2, while in the second approach, the effect of stirring rate (400 and 600 rpm) was studied under the same reaction conditions, using 50% *w/v* surrogate mixture in *n*-hexadecane. In the first series of experiments, complete conversion of the surrogate mixture compounds was observed only by using the 5% *w/v* mixture in *n*-hexadecane, yielding 27.9% cyclohexane, 36.6% methyl-cyclohexane, and 4.8% methyl-cyclopentane. The rest of the products (30%) were alkyl-cycloalkanes (cyclopentanes and cyclohexanes) substituted with more than one alkyl group and with chains of different carbon numbers (methyl,

ethyl, propyl, and combinations), as well as some dimers (1,1'-methylenebis-cyclohexane, 1,1'-Bicyclohexyl, (cyclopentylmethyl)-cyclohexane), mainly identified by GC-MS analysis. An increase in the surrogate mixture concentration in the feed to 25% *w/v* led to a slight decrease in the conversion to 94% but a substantial decrease in the cycloalkane yield from 69.5% to 41.3% (16.4% cyclohexane, 21.4% methyl-cyclohexane, 1.0% ethyl-cyclohexane, and 2.5% methyl-cyclopentane). Further increase of the concentration to 50% *w/v* led to a relatively high conversion (90%) but an even lower cycloalkane yield (25.5%; 7.8% cyclohexane, 14.6% methyl-cyclohexane, 1.2% ethyl-cyclohexane, and 1.9% methyl-cyclopentane), as can be observed in Figure 4. The above results were also confirmed by the GC-MS analysis, which showed that at the two higher feed concentrations, the relative abundance of the remaining unconverted phenolics and aromatics was substantially high (Figure 5). Further insight was offered by the second series of experiments, i.e., via increasing the stirring rate from 400 rpm to 600 rpm. As shown in Figure 4, the yield of total non-oxygenated compounds increased from 29% (at 400 rpm) to 67.6% (at 600 rpm), comprising 25.2% cyclohexane, 42.2% methyl-cyclohexane, 1.5% ethyl-cyclohexane, and 2.7% methyl-cyclopentane. Considering that the conversion is almost similar at both stirring rates, it can be assumed that a mass-transfer limitation of the intermediate products takes place, thus hindering complete hydrodeoxygenation/hydrogenation to alkyl-cyclohexanes. Still, in order to elucidate whether the decreased hydrodeoxygenation efficiency is attributed to external mass-transfer limitations or internal diffusion within the zeolite particles or even to inhibited hydrogen gas diffusion due to the nature (relatively high viscosity) of lignin bio-oil surrogate, more dedicated kinetic studies are required [72–74].

2.4. Carbon/Coke Quantification of Used Catalysts

Spent catalysts were characterized by various techniques to examine the possible deactivation due to coke formation. All spent catalysts exhibited carbon contents in the range of 3–8 wt.%, except for the experiment where hydrogen was consumed without adding extra hydrogen to keep the pressure stable, as can be observed in Figure 7. Elemental analysis provides the total carbon content of catalysts as well as an indication of coke hardness via the H/C ratio. On the other hand, thermogravimetric analysis (TGA) can be used for the quantification of coke. Overall, the carbonaceous depositions on the catalyst can be attributed to both chemisorbed organic compounds and coke deriving from the oligomerization of aromatic and phenolic compounds.

Regarding the effect of hydrogen pressure, in the experiment where the hydrogen was consumed during the reaction, the carbon content exhibited the highest value of $C_{\text{elemental}} = 24.6$ wt.%. Furthermore, the total mass loss accounted for 42.6 wt.% based on catalyst (11.3 wt.% on feed). The main weight loss (37.1 wt.%) is in the temperature range of 80–250 °C ($T_{\text{max}} = 195$ °C), as can be observed in the TGA analysis of Figure S6 and Table S1, and is attributed to adsorbed hydrocarbons. At higher temperatures of 250–600 °C ($T_{\text{max}} = 383$ and 452 °C), the weight loss is lower at 2.9 and 2.6 wt.% and is attributed to coke deposition. Keeping the hydrogen pressure stable during the experiment led to a substantial decrease in carbon content $C_{\text{elemental}} = 3.6$ wt.% due to the higher hydrogenation/deoxygenation efficiency, thus minimizing the presence of phenolics and aromatics that could serve as coke precursors. Based on the thermogravimetric analysis, the total mass loss was 13.9 wt.% (3.2 wt.% on feed), and the weight loss occurred in four distinct steps. The first mass loss (6.1 wt.%) took place below 200 °C ($T_{\text{max}} = 78$ °C) and was attributed to the remaining solvent. The second weight loss (2.3 wt.%) was in the temperature range of 200–300 °C ($T_{\text{max}} = 254$ °C) and was due to the degradation of adsorbed light hydrocarbons. The third step of weight loss (2.8 wt.%) was observed at 300–400 °C ($T_{\text{max}} = 350$ °C) and was due to the burning of soft coke, which can be easily

burnt at lower temperatures. The last step of weight loss (2.5 wt.%) was at temperatures of >400 °C ($T_{\max} = 409$ °C) and was attributed to hard or graphitized coke. These results are in accordance with similar studies in the literature where coke depositions have been determined via TGA in spent catalysts [75,76]. Increasing the initial hydrogen pressure from 50 to 70 bar had a minor effect, with a small increase in the total carbon content from $C_{\text{elemental}} = 3.6$ to 5.6 wt.%. Considering the H/C ratio (Figure S7), the increase in the initial pressure from 50 to 70 bar led to a decrease in the H/C ratio from 0.44 to 0.31. The decrease in the H/C ratio can be attributed to heavier aromatic compounds that can be condensed during coke formation [77].

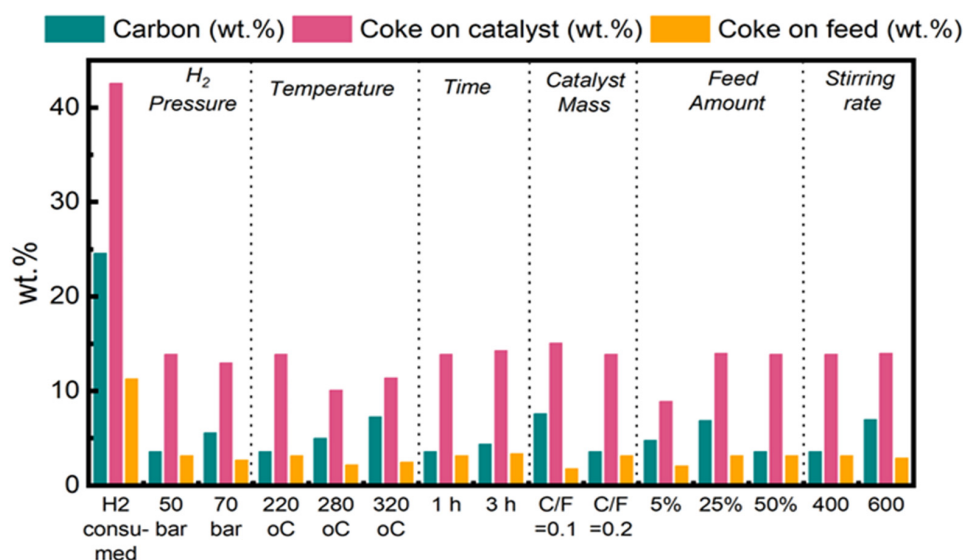


Figure 7. Effect of different reaction conditions on carbon (elemental analysis)/coke (TGA) depositions on 10%Ni/BETA (12.5).

Regarding the effect of the reaction temperature, the increase from 220 °C to 320 °C led to a gradual increase in the carbon content from $C_{\text{elemental}} = 3.6$ wt.% (220 °C) to 5.0 wt.% (280 °C) and 7.6 wt.% (320 °C) and a decrease in the H/C ratio from 0.44 to 0.16. The harder nature of coke is also confirmed via thermogravimetric analysis. The higher reaction temperature induced a decrease in mass loss at lower temperatures (<200 °C and 200–300 °C), at the same time shifting the T_{\max} of the weight loss steps at 300–600 °C towards higher temperatures, $T_{\max} = 350$ °C (at 220 °C) to $T_{\max} = 428$ °C (at 280 °C) and $T_{\max} = 487$ °C (at 320 °C), as shown in Table S1 and Figure S6. The prolonged reaction time (3 h) also had a slight effect, increasing the carbon content from $C_{\text{elemental}} = 3.6$ wt.% (at 1 h) to 4.4 wt.% (at 3 h) and decreasing the H/C ratio from 0.44 to 0.37. Still, the thermogravimetric analysis did not show any weight loss in the temperature range of 400–600 °C but a clear increase in the weight loss in the low temperature ranges (200–300 °C and 300–400 °C), proving that the carbon deposition is attributed to the higher amount of adsorbed hydrocarbons and soft coke.

The lower ratio of active sites ($C/F = 0.1$) resulted in lower conversion and cycloalkane yields, as shown in Section 2.3. The lower activity led to a higher carbon content on the catalyst of $C_{\text{elemental}} = 7.6$ wt.% ($C/F = 0.1$), compared to 3.6 wt.% at $C/F = 0.2$. The TGA data revealed that the weight losses at 200–300 °C and 400–600 °C ($T_{\max} = 279$ °C, 4.7 wt.% and $T_{\max} = 433$ °C, 3.0 wt.%) are higher with $C/F = 0.1$ compared to those with $C/F = 0.2$ ($T_{\max} = 254$ °C, 2.3 wt.% and $T_{\max} = 409$ °C, 2.5 wt.%), as shown in Table S1. These results indicate that the lower C/F ratio enhanced the chemisorption of light hydrocarbons and coke formation of a more condensed nature, as also observed via the H/C ratio based on elemental analysis. The carbon content and deposited hydrocarbons and coke were also

increased upon increasing the relative concentration of the surrogate mixture in the feed. Finally, regarding the stirring rate, the higher hydrodeoxygenation efficiency at 600 rpm led to an increase in carbon content from $C_{\text{elemental}} = 3.6$ wt.% (400 rpm) to 7.0 wt.% (600 rpm). The total carbonaceous deposits (from TGA) were similar for both stirring rates, equal to 14 wt.% (≈ 3 wt.% on feed), but the different stirring conditions led to different types of deposits. The lower stirring rate slightly enhanced the formation of soft and hard coke, showing higher weight losses at 300–400 °C and 400–600 °C, i.e., $T_{\text{max}} = 350$ °C, 2.8 wt.% and $T_{\text{max}} = 409$ °C, 2.5 wt.% compared to $T_{\text{max}} = 357$ °C, 2.2 wt.% and $T_{\text{max}} = 418$ °C, 2.1 wt.%, while the higher stirring rate mainly induced the accumulation of adsorbed light hydrocarbons ($T_{\text{max}} = 243$ °C, 3.3 wt.% vs. $T_{\text{max}} = 254$ °C, 2.3 wt.%).

2.5. Structural, Porosity, and Surface Characteristics of Used and Regenerated Catalysts

Selected spent catalysts were characterized via the following methods: i. XRD analysis to identify any changes in their crystallinity and structure, ii. N_2 physisorption to examine deterioration of the porous properties, iii. FTIR with in situ pyridine adsorption for determination of the amount and type of acid sites, and iv. XPS analysis to investigate changes on the catalyst surface. Afterwards, the spent catalysts were regenerated (calcination under air followed by reduction in hydrogen flow) and were characterized via the above-mentioned techniques to examine whether they retained the properties of the parent, fresh catalysts. The catalyst selection was based on the severity of the hydrodeoxygenation conditions as well as their activity. Thus, the catalysts selected were derived from the experiments, as follows: higher reaction temperature (320 °C, 1 h, 50 bar H_2 , C/F = 0.2, 50%, 400 rpm), prolonged reaction time (220 °C, 3 h, 50 bar H_2 , C/F = 0.2, 50%, 400 rpm) and higher stirring rate (220 °C, 1 h, 50 bar H_2 , C/F = 0.2, 50%, 600 rpm).

2.5.1. XRD Results

The stability of the active metallic and acidic sites were examined via XRD and FTIR-Pyr spectroscopy. More specifically, the maintenance of the metallic phase of nickel and the crystallinity of the support were examined via XRD analysis. As can be observed in the patterns of Figure 8, the metallic phase of nickel is maintained in the spent catalysts, and no peaks attributed to nickel oxides were observed. Furthermore, limited sintering of metallic Ni was observed, leading to a slight increase in the crystallite size of nickel (D_{Ni} , Table 1) from 14 to 15–16 nm. Regarding the crystallinity of the catalysts, no substantial change/decrease was observed. To this end, regeneration of the catalysts did not have an additional effect on crystallinity. The nickel crystallite size of the regenerated catalysts was estimated to be 12–16 nm.

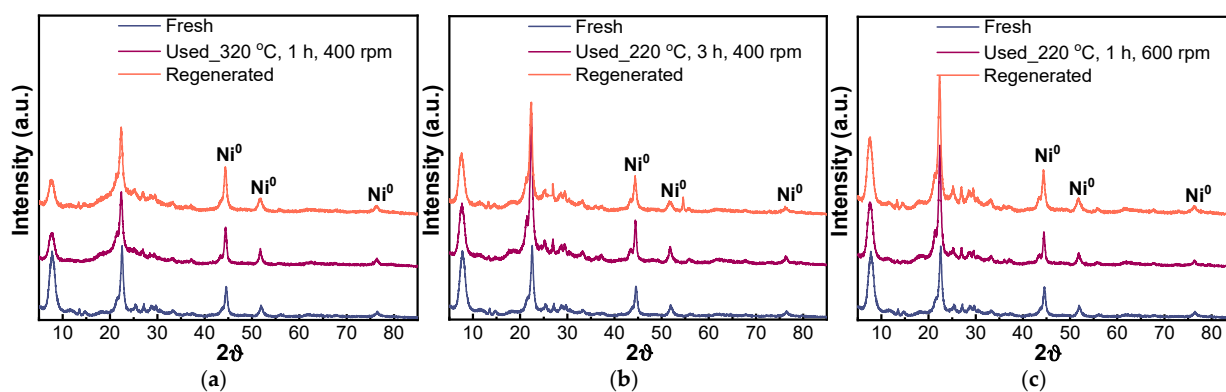


Figure 8. XRD analysis of selected spent and regenerated catalysts recovered from the experiments at (a) 320 °C, 1 h, 50 bar H_2 , C/F = 0.2, 50% surrogate in hexadecane, 400 rpm, (b) 220 °C, 3 h, 50 bar H_2 , C/F = 0.2, 50% surrogate in hexadecane, 400 rpm and (c) 220 °C, 1 h, 50 bar H_2 , C/F = 0.2, 50% surrogate in hexadecane, 600 rpm.

Table 1. Textural characteristics and acidity of used and regenerated catalysts.

Catalyst	D_{Ni}^1 (nm)	S_{BET}^2 (m^2/g)	S_{micro}^3 (m^2/g)	S_{mm}^4 (m^2/g)	V_{total}^5 (cm^3/g)	V_{micro}^3 (cm^3/g)	Bronsted ⁶ ($\mu mol/g$)	Lewis ⁶ ($\mu mol/g$)	B/L
10%Ni/BETA (12.5)	14	562	371	191	1.151	0.154	102	182	0.56
320 °C, 1 h, 50 bar H ₂ , C/F = 0.2, 50%, 400 rpm	15	169	65	104	1.009	0.029	18	74	0.24
Regenerated	12	306	213	92	1.143	0.092	50	126	0.40
220 °C, 3 h, 50 bar H ₂ , C/F = 0.2, 50%, 400 rpm	16	497	340	157	1.208	0.148	19	264	0.07
Regenerated	12	474	343	131	1.037	0.149	78	251	0.31
220 °C, 1 h, 50 bar H ₂ , C/F = 0.2, 50%, 600 rpm	16	419	266	153	0.945	0.115	53	262	0.20
Regenerated	18	507	337	170	1.059	0.146	42	149	0.28

¹ Determined via XRD analysis and the Scherrer equation, ² Calculated via the multipoint BET equation from N₂ sorption at −196 °C, ³ Calculated via the t-plot method, ⁴ Meso/macropore and external area estimated as the difference of the total (BET) minus micropore area, ⁵ Total pore volume at P/P₀ = 0.99, ⁶ Bronsted and Lewis acid site amounts determined via FTIR-Pyr spectroscopy.

2.5.2. XPS Results

Further characterization of the structure and composition of the catalysts' surfaces was conducted via XPS. The assigned peaks and their relative contribution are summarized in Table 2. The analysis of the catalyst recovered from the optimum experimental conditions (220 °C, 1 h, 50 bar H₂, C/F = 0.2, 50%, 600 rpm) is shown in Figure 9 and is compared to the fresh catalyst. In the wide scan, the elements C, Si, O, Ni, and Al were identified on the surface of fresh Ni/BEA, as shown in Figure 9a. The assignments of peaks were based on similar literature data [78–80]. Regarding the region 845–905 eV associated with nickel, the peak at 855.5 eV is attributed to Ni 2p_{3/2} and the peak at 875.5 eV to Ni 2p_{1/2}, in relation to the Ni⁺² oxidation state and the crystal structure of Ni(OH)₂. This hydroxide is formed due to the physically adsorbed moisture on the surface of the catalyst. Also, the sensitive surface of the catalyst led to the peak of O 1s at 531.1 eV due to the presence of oxygen bonds with Al and Ni, while the peak Al 2p at 75.4 eV is due to the presence of aluminum hydroxides formed due to moisture, mostly on extra-framework aluminum species (Figure S8a). The carbon peaks at 531.8 and 534.1 eV are attributed to C–O and C=O bonds due to the adsorption of carbon dioxide. The strong signal of Si–O at 103.9 eV (Figure S8a) is due to the silica-rich zeolite support, while the Si/Al ratio was estimated to be 19.5, slightly higher than the bulk Si/Al ratio of zeolite beta. Upon etching of the catalyst surface by 10 nm, a few surface layers were removed and revealed the presence of metallic Ni (Ni 2p_{1/2} at 869.9 eV and Ni 2p_{3/2} at 852.7 eV), while the peaks attributed to Ni²⁺ were not identified. These results are in accordance with the XRD analysis, which clearly confirmed the metallic phase of nickel in the bulk phase of the catalyst. Carbon peaks exhibited significantly lower intensity, while Si 2p and Al 2p peaks at 103.6 and 75.5 eV are associated with the zeolite structure. The Si/Al ratio was estimated at 21.9.

Regarding the XPS spectrum of the used catalyst, shown in Figure 9b, the wide scan confirmed the presence of C, Si, O, Ni, and Al. Focusing on the metallic nickel phase, the Ni 2p_{3/2} peak is centered at 853 eV, while peaks of lower intensity attributed to Ni 2p_{3/2} of Ni²⁺ and Ni 2p_{3/2} of Ni³⁺ due to the NiOOH structure were identified at 854 and 857 eV, respectively (Figure 9b, middle), in accordance with similar studies from the literature. The contribution of the NiO structure was calculated to be 36.6%, while the contribution of NiOOH structure was calculated to be 63.4%. The ratio of oxidation states Ni²⁺/Ni³⁺ was estimated to be 0.58. Carbon depositions formed due to the adsorption of organic compounds, and coke led to multiple peaks (Figure 9b, right). The peak at

284.6 eV is attributed to the C 1s and C-C bonds due to the aliphatic carbon depositions [75]. Coke depositions on the metal active sites were also observed at 283.5 eV, attributed to the C 1s and C-metal interactions. Furthermore, the peaks at 286, 287.5, and 289.4 eV were assigned to C-O, O-C=O, and CO-OH bonds, most probably attributed to the carboxylic acids, ether, and alcohols of the intermediate compounds sorbed on the catalyst surfaces. The relative content of each peak is 45.6% for C-C, 30.1% for C-O, 12.7% for O-C=O, 3.7% for CO-OH, and 7.9% for C-metal interactions. The Si 2p spectra reveal two distinct peaks, indicative of silicon environments commonly found within zeolite materials. The peak of Si-O bonds within the zeolite framework centered at 103.5 eV exhibited a 71.7% contribution, while the remaining 28.3% was attributed to the Si-Al bonds centered at 104.4 eV (Figure S8b). Similarly, the Al 2p spectrum reveals two primary peaks, consistent with the expected aluminum environments in zeolites. The peak at 74.5 eV is attributed to the Al-O-Si of the zeolite framework with a 36.7% contribution, while the peak at 75.6 eV is due to the Al-O bonds with a 63.3% contribution. The Si/Al ratio was estimated to be 12.9. Those assumptions were confirmed by the oxygen peaks. Oxygen interactions with carbon were confirmed via the peaks at 532 and 533.5 eV corresponding to C=O and C-O bonds, with relative contributions of 16.9% and 37.1%, respectively. The hydroxyl groups were confirmed at 534.7 eV, with a 5.7% contribution. The metal-oxygen bonds due to metal oxides were assigned to 531 eV, with a 3.3% contribution, while the peak of the Si-O bonds was centered at 532.8 eV, with a 37% relative contribution.

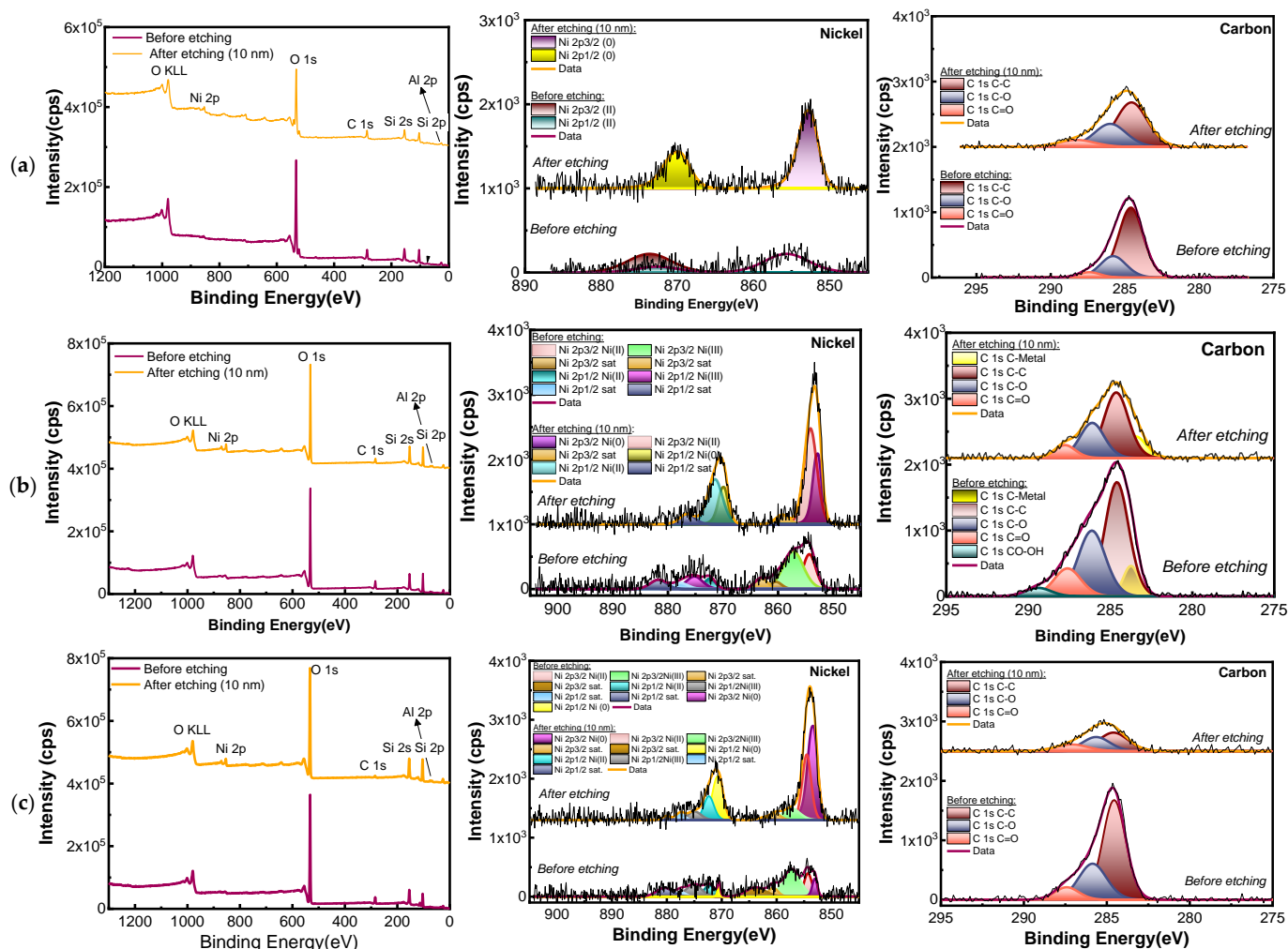


Figure 9. XPS spectra of (a) fresh, (b) used, and (c) regenerated catalyst from the experiment at 220 °C, 1 h, 50 bar H₂, C/F = 0.2, 50%, 600 rpm. Left: wide spectra, middle: nickel region, and right: carbon region.

Table 2. Assignment of XPS peaks and relative contribution of each phase.

Peak	Peak Energy (eV)	Relative Contribution					
		Fresh		Used		Regenerated	
		Before Etching	After Etching	Before Etching	After Etching	Before Etching	After Etching
Nickel							
Ni2p3/2, Ni ⁰	853.0 ± 0.3	0.0%	61.9%	0.0%	34.5%	11.2%	56.1%
Ni2p3/2, Ni ²⁺	854.3 ± 0.2	76.7%	0.0%	36.6%	65.5%	28.6%	32.1%
Ni2p3/2, Ni ³⁺ , Ni(OOH)	857.3 ± 0.2	0.0%	0.0%	63.4%	0.0%	60.2%	11.8%
Ni2p1/2, Ni ⁰	869.9 ± 0.3	0.0%	38.1%	0.0%	0.0%	0.0%	0.0%
Ni2p1/2, Ni ²⁺	872.5 ± 0.2	23.3%	0.0%	0.0%	0.0%	0.0%	0.0%
Ni2p1/2, Ni ³⁺	875.4 ± 0.2	0.0%	0.0%	0.0%	0.0%	0.0%	0.0%
Silicon							
Si2p, Si-O in zeolite	103.5 ± 0.2	100%	100%	71.7%	71.7%	57.7%	23.9%
Si2p, Si-Al in zeolite	104.4 ± 0.2	0%	0%	28.3%	28.3%	42.3%	76.1%
Aluminum							
Al2p, Al-O-Si, in zeolite	74.5 ± 0.2	0.0%	0.0%	36.7%	36.0%	10.8%	7.8%
Al2p, Al-O, in oxides	75.6 ± 0.2	100%	100%	63.3%	64.0%	89.2%	33.4%
Al2p, Al ³⁺	76.6 ± 0.2	0.0%	0.0%	0.0%	0.0%	0.0%	58.8%
Carbon							
C1s, C-C	284.6 ± 0.2	71.9%	58.4%	45.6%	50.3%	63.6%	47.3%
C1s, C-O	286.0 ± 0.2	23.2%	31.0%	30.1%	26.9%	28.0%	33.9%
C1s, O-C=O	287.5 ± 0.2	4.9%	10.6%	12.7%	8.4%	8.4%	18.7%
C1s, CO-OH	289.4 ± 0.2	0.0%	0.0%	3.7%	0.0%	0.0%	0.0%
C1s, C-metal	283.5 ± 0.2	0.0%	0.0%	7.9%	14.4%	0.0%	0.0%
Oxygen							
O1s, C=O	532.0 ± 0.2	4.3%	4.0%	16.9%	16.0%	6.5%	9.2%
O1s, C-O	533.5 ± 0.2	5.0%	6.2%	37.1%	26.4%	35.4%	41.3%
O1s, -OH	534.7 ± 0.2	11.2%	12.2%	5.7%	4.9%	14.5%	23.4%
O1s, moisture	536.4 ± 0.2	0.0%	0.0%	0.0%	0.0%	11.1%	0.0%
O1s, O-metal	531.0 ± 0.2	2.7%	4.7%	3.3%	8.6%	2.7%	2.0%
O1s, Si-O	532.8 ± 0.2	76.9%	72.9%	37.0%	44.0%	29.7%	24.0%

After etching of the surface by 10 nm, the peak corresponding to Ni 2p3/2 of metallic nickel was centered at 853 eV, and the peak of Ni 2p3/2 of Ni²⁺ at 854.3 eV. The etching process eliminated Ni(III) species. The relative content of each phase was 34.5% Ni⁰ and 65.5% Ni²⁺, proving that the bulk phase exhibited a higher content of metallic nickel compared to the outer surface, in accordance with the analysis of the fresh catalyst. Differences were also observed in the carbon interactions. Notably, the peak at 289.4 eV due to CO-OH disappeared after etching, suggesting that it originated from a surface contaminant. The remaining peaks of carbon interactions were maintained after etching. C-C (284.6 eV) exhibited a 50.3% relative contribution, C-O bonds (286 eV) exhibited a 26.9% relative contribution, O-C=O bonds (287.5 eV) exhibited an 8.4% relative contribution, and C-metal (283.5 eV) exhibited a 14.4% contribution. The peak of Si 2p attributed to Si-O and Si-Al bonds remained relatively stable after etching, indicating a minimal change in the chemical state of silicon (Figure S8b, middle). Similarly, for the Al 2p spectra, the peak centered at 74.5 eV is attributed to Al-O-Si, with a 36% relative contribution, while the peak at 75.6 eV is due to the Al-O bonds, with a 64% contribution. Finally, the analysis of O 1s peaks after etching confirmed the C=O bonds at 532 eV with a 16% contribution, the C-O bonds at 533.5 eV with a 26.4% contribution, the hydroxy groups at 534.7 eV with a 4.9% contribution, the metal-oxygen interactions due to metal oxide presence at 531 eV with an 8.6% contribution, and the Si-O bonds at 532.8 eV with the highest contribution, 44%.

The regeneration of the used Ni/BEA catalyst resulted in significant changes in the catalyst's surface structure. The regeneration process led to the recovery of the metallic phase of nickel, as can be observed via the Ni 2p3/2 of Ni⁰ peak centered at 853 eV,

while the Ni^{2+} and Ni^{3+} phases at 854 and 857 eV exhibited 28.6% and 60.2% relative contributions, respectively. The ratio of $\text{Ni}^{2+} / \text{Ni}^{3+}$ was estimated to be equal to 0.47, and the ratio of $\text{Ni}^0 / \text{Ni}^{2+}$ equal to 0.39 (Figure 9c, middle). The most significant changes were observed in the peaks attributed to carbonaceous compounds. The peaks attributed to CO-OH and the C-metal interactions bonds disappeared after regeneration of the catalyst, while the peaks of C-O and O-C=O were identified at 286 and 287.5 eV, but with lower relative contents, 28% and 8.4%, compared to the used catalyst. On the other hand, the peak at 284.6 eV corresponding to C-C bonds of coke depositions remained in the regenerated catalyst, and its relative content increased to 63.6%. This trend revealed that the applied calcination-reduction treatment of the spent catalyst was an efficient process for the removal of the adsorbed phenolic/aromatic compounds but proved to be insufficient for the removal of hard coke. The Si 2p spectrum revealed two distinct peaks, indicative of silicon environments in zeolite. The Si-O bond with the zeolite framework is responsible for the peak centered at 103.5 eV, while the peak at 104.4 eV is due to the Si-Al bond (Figure S8c). The relative contribution of Si-O is 57.7%, lower compared to the spent catalyst, while the Si-Al content is 42.3%, significantly higher than in the spent catalyst. The same trend was revealed by the Al 2p spectra analysis. The Al-O-Si bond within the zeolite framework is responsible for the peak at 74.5 eV, which exhibited a 10.8% relative contribution compared to the used catalyst, while the Al-O content increased to 89.2%, which indicates a decrease in the aluminum amount incorporated within the zeolite framework. The deconvoluted O 1s spectrum revealed the distinct oxygen bonding environments, the majority of which originated from surface contamination, as suggested by the C 1s analysis, such as the C=O bonds at 532 eV, the C-O bonds at 533.5 eV, and the OH groups 534.7 eV. The relative contribution of each group is 6.5% for C=O, 35.4% for C-O, and 14.5% for the OH group. Furthermore, in the regenerated catalyst, a peak at 536.4 eV was observed due to the adsorbed moisture, comprising 11.1% of the total oxygen signal. Compared to the used catalyst, the oxygen bond in metal oxides at 531 eV exhibited a slightly lower contribution of 2.7%, as well as the Si-O bond at 532.8 eV with a 29.7% contribution. The Ar^+ ion etching process revealed that the dominant state of nickel is the metallic nickel with a 56.1% contribution, while the crystal structures corresponding to Ni^{2+} significantly decreased to 32.1% compared to the surface before etching as well as to the used catalyst (Figure 9c, middle). The $\text{Ni}^0 / \text{Ni}^{2+}$ ratio was estimated to be equal to 1.75. In the C 1s spectrum, the main bonds identified after etching were the C-C bond at 284.6 eV with a 47.3% relative contribution, the C-O bond at 286 eV with a 33.9% relative contribution, and the O-C=O bond at 287.5 eV with an 18.7% contribution. Regarding the Si 2p spectrum, a significant shift is observed in the peak at 104.5 eV of Si-Al, proving that the bond of the zeolite is the dominant phase, with a 76.1% relative contribution. In the Al 2p spectrum, multiple bonds were identified, including the Al-O-Si bond at 74.5 eV with 7.8% contribution, the Al-O bonds at 75.6 eV with 33.4% contribution, and a new oxidation state of aluminum, Al^{3+} , the phase of which exhibits 58.8% contribution. The Si/Al ratio was estimated to be 11.55. The above observations were also confirmed via the analysis of the O 1s spectrum. The peaks corresponding to organic compounds were identified at 532 eV (C=O), with a 9.2% contribution, and at 533.5 eV (C-O), with a 41.3% contribution. The peak at 534.7 eV was assigned to hydroxyl groups, with a 23.4% contribution, while the peak at 531 eV was assigned to the metal-oxygen bonds, with a 2% contribution. Finally, the Si-O bonds at 532.8 eV led to a 24% relative contribution.

The *main conclusions of the XPS analysis are as follows*. The nickel oxidation state changed from Ni^0 to Ni^{2+} and Ni^{3+} during the hydrodeoxygenation of the surrogate mixture, while the regeneration of the spent catalyst enhanced the reduction of $\text{Ni}^{2+} / \text{Ni}^{3+}$ to Ni^0 to a great extent. The carbonaceous depositions, either in the form of coke or unconverted

adsorbed oxy-phenolic and oxy-aromatic compounds, led to multiple peaks in the XPS spectrum of the used catalyst. The regeneration process burnt the carbonaceous deposits on metal but retained the hard coke formed during the hydrodeoxygenation, as well as the oxygen-containing compounds. Additionally, slight changes were observed in the zeolite framework and the formation of Al^{3+} extra-framework (EFAL) species, which is usually observed in zeolites due to skeletal dealumination and the formation of EFAL species upon reaction and subsequent regeneration upon calcination.

2.5.3. Acidity Results

Regarding the acid sites of the spent and regenerated catalysts, they were determined via FTIR spectroscopy with in situ adsorption of pyridine. Brønsted acid sites proved to be the most vulnerable to deactivation compared to Lewis acid sites. In general, both the number of Brønsted acid sites and the B/L ratio were drastically reduced in spent catalysts, as can be observed in Table 1. The harder nature of coke formed upon hydrodeoxygenation of the surrogate mixture at 320 °C led to a tremendous decrease in the total acid sites (B+L) from 284 $\mu\text{mol/g}$ to 92 $\mu\text{mol/g}$ and especially lowered the Brønsted acid sites from 102 $\mu\text{mol/g}$ to 18 $\mu\text{mol/g}$, as well as the B/L ratio from 0.56 to 0.24. The regeneration of that catalyst led to partial recovery of both Brønsted and Lewis acid sites, resulting in an increase in the B/L ratio from 0.24 to 0.4. These results show that the above reaction conditions do not lead to permanent destruction of Brønsted acid sites, which can be recovered to a great extent. The hydrodeoxygenation at 220 °C, but for a longer reaction time, led to a similar substantial decrease in Brønsted acid sites from 102 $\mu\text{mol/g}$ to 19 $\mu\text{mol/g}$ but induced an increase in Lewis acid sites from 182 $\mu\text{mol/g}$ to 264 $\mu\text{mol/g}$, keeping the total acidity stable. The increase in Lewis acid sites is indicative of the partial conversion of Brønsted zeolitic sites to Lewis acid sites via skeletal dealumination and the formation of extra-framework AL (EFAL) species that may act as Lewis acid sites [81–84]. The softer nature of coke compared to the coke formed at higher reaction temperatures favored the greater recovery of Brønsted acid sites during the regeneration, resulting in an increase in the B/L ratio from 0.07 to 0.31. The lowest decrease in acid sites was observed in the optimal catalytic system (220 °C, 1 h, 50 bar H_2 , C/F = 0.2, 50%, 600 rpm). The Brønsted acid sites decreased from 102 $\mu\text{mol/g}$ to 53 $\mu\text{mol/g}$, while the Lewis acid sites increased from 182 $\mu\text{mol/g}$ to 262 $\mu\text{mol/g}$. However, the regeneration of this catalyst did not favor the recovery of Brønsted acid sites, keeping the B/L ratio low and almost similar to that of the used catalyst. This fact can be correlated with the presence of extra-framework Al^{3+} , identified in the XPS analysis of the regenerated catalyst, and maybe this is an indication that the Brønsted acid sites are permanently converted to Lewis acid sites, as also observed for the regeneration of similar catalysts [85].

2.5.4. Porosity Results

The porous properties of the catalyst were examined via N_2 physisorption. The isotherms and the BJH pore-size distributions of the spent and regenerated catalysts are shown in Figure 10, and the results are given in Table 1. The severity of the hydrodeoxygenation process significantly influenced the porous properties. The most profound effect on the porous properties resulted from the increase in the reaction temperature. The higher reaction temperature resulted in a tremendous decrease in the specific surface area from $S_{\text{BET}} = 562 \text{ m}^2/\text{g}$ (fresh catalyst) to 169 m^2/g and total pore volume from $V_{\text{total}} = 1.151 \text{ cm}^3/\text{g}$ to 1.009 cm^3/g . Considering the microporous characteristics, S_{mic} exhibited an 82% decrease from $S_{\text{mic}} = 371 \text{ m}^2/\text{g}$ to 65 m^2/g , while the meso/macroporous area exhibited only a 45% decrease from $S_{\text{mm}} = 191 \text{ m}^2/\text{g}$ to 104 m^2/g . Similarly, the volume of micropores decreased substantially from $V_{\text{micro}} = 0.154 \text{ cm}^3/\text{g}$ to 0.029 cm^3/g .

These values show that the deposited coke induced the blocking and/or destruction of the micropores and affected the meso/macroporous network of the zeolite support to a lesser extent, in accordance with literature results [86]. On the other hand, the prolonged reaction time resulted in a limited decrease in the specific surface area from $S_{\text{BET}} = 562 \text{ m}^2/\text{g}$ (fresh catalyst) to $497 \text{ m}^2/\text{g}$, while the total pore volume was almost similar. Compared to the reaction temperature, the prolonged reaction time did not influence the microporous area, which decreased slightly from $S_{\text{mic}} = 371 \text{ m}^2/\text{g}$ to $340 \text{ m}^2/\text{g}$, while the meso/macroporous area exhibited an 18% decrease from $S_{\text{mm}} = 191 \text{ m}^2/\text{g}$ to $157 \text{ m}^2/\text{g}$, proving that the higher reaction time favored the deposition of coke on the outer surface of the catalysts or within the mesopores of the zeolite. Regarding the more active catalytic system ($220 \text{ }^\circ\text{C}$, 1 h, 50 bar H_2 , $C/F = 0.2$, 50%, 600 rpm), the spent catalyst exhibited only a 25% decrease in the surface area from $S_{\text{BET}} = 562 \text{ m}^2/\text{g}$ to $419 \text{ m}^2/\text{g}$, while the total pore volume decreased from $V_{\text{micro}} = 0.154 \text{ cm}^3/\text{g}$ to $0.115 \text{ cm}^3/\text{g}$. The microporous area exhibited an almost equal decrease to the meso/macroporous area. The microporous area decreased from $S_{\text{mic}} = 371 \text{ m}^2/\text{g}$ to $266 \text{ m}^2/\text{g}$, while the meso/macroporous decreased from $S_{\text{mm}} = 191 \text{ m}^2/\text{g}$ to $153 \text{ m}^2/\text{g}$.

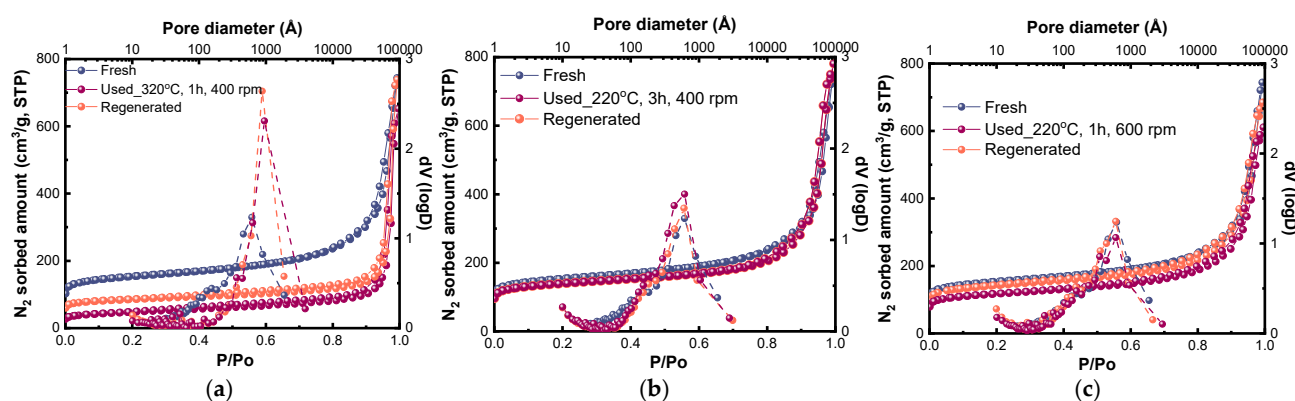


Figure 10. N_2 physisorption isotherms and BJH pore-size distributions of selected spent and regenerated catalysts recovered from the experiments at (a) $320 \text{ }^\circ\text{C}$, 1 h, 50 bar H_2 , $C/F = 0.2$, 50% surrogate in hexadecane, 400 rpm, (b) $220 \text{ }^\circ\text{C}$, 3 h, 50 bar H_2 , $C/F = 0.2$, 50% surrogate in hexadecane, 400 rpm and (c) $220 \text{ }^\circ\text{C}$, 1 h, 50 bar H_2 , $C/F = 0.2$, 50% surrogate in hexadecane, 600 rpm.

Upon regeneration via calcination and subsequent reduction, the used catalyst from the experiment at $320 \text{ }^\circ\text{C}$ containing the highest amount of hard coke deposition exhibited substantial recovery of its porous characteristics (Figure 10a). More specifically, the surface area increased from $S_{\text{BET}} = 169 \text{ m}^2/\text{g}$ (in the used sample) to $306 \text{ m}^2/\text{g}$ (after regeneration), while the total pore volume increased from $V_{\text{total}} = 1.009 \text{ cm}^3/\text{g}$ to $1.143 \text{ cm}^3/\text{g}$. The recovery of the porous characteristic is mainly attributed to the regeneration of microporous characteristics compared to meso/macropores. The microporous area exhibited a significant increase from $S_{\text{mic}} = 65 \text{ m}^2/\text{g}$ to $213 \text{ m}^2/\text{g}$, while the meso/macroporous area remained almost similar, as shown in Table 1, indicating that the initial decrease in the micro-area was mainly due to micropore blockage and not actual destruction of the micropore network. On the other hand, the regeneration of the catalyst obtained after the prolonged reaction time experiment with much less deterioration of its porosity exhibited similar porosity characteristics to those of the spent sample, close to those of the parent, fresh catalyst (Figure 10b, Table 1). In the case of the experimental conditions leading to the highest hydrodeoxygenation activity, the regeneration of the catalyst led to a substantial increase in the surface area from $S_{\text{BET}} = 419 \text{ m}^2/\text{g}$ to $507 \text{ m}^2/\text{g}$ as well as of the total pore volume from $V_{\text{total}} = 0.945 \text{ cm}^3/\text{g}$ to $1.059 \text{ cm}^3/\text{g}$, values that are very close to those of the fresh catalyst (Figure 10c, Table 1).

Based on the characterization of spent catalysts, it can be highlighted that the severity of the reaction conditions variably influenced the physicochemical properties of the used and regenerated catalysts. The different nature of the carbonaceous species (adsorbed organics, soft coke, hard coke), as well as the topology of depositions (metal sites, acid sites, outer surface, pore channels), led to different deactivation extents. Furthermore, the regeneration process, which involves calcination of spent catalysts under air, aiming to burn the carbonaceous species, followed by reduction under hydrogen flow to obtain the metallic phase of nickel, proved to be an efficient process for partial or almost complete recovery of the physicochemical and acidic properties of the catalysts, depending on the extent of their initial deactivation.

3. Materials and Methods

3.1. Catalyst Preparation and Characterization

BETA zeolite with Si/Al = 12.5 was obtained from Zeolyst and used as the catalyst support. Prior to the impregnation, the support was calcined at 500 °C for 3 h to convert the ammonium form into proton form. The catalyst, 10%Ni/BETA (12.5), was synthesized via the incipient wetness impregnation method. In this procedure, a specific amount of nickel precursor, $\text{Ni}(\text{NO}_3)_2 \cdot 6\text{H}_2\text{O}$, corresponding to 10 wt.% Ni, was dissolved in a certain amount of deionized water that was equal to the total pore volume of the support. Then, the aqueous solution was added dropwise to the support and grounded in a mortar. Afterwards, the solid was dried at 100 °C and calcined at 500 °C for 3 h at a 2 °C/min heating rate. Prior to the catalytic experiments, the catalyst was reduced at 450 °C for 3 h under 50 mL/min H_2 flow.

Fresh and spent catalysts were characterized via X-ray powder diffraction (XRD), N_2 porosimetry, FTIR with in situ adsorption of pyridine, and X-ray photoelectron spectroscopy (XPS). XRD analysis was performed using a Rigaku Ultima+ 2cycles X-ray diffractometer with CuK α X-ray radiation over a $2\theta = 5\text{--}85^\circ$ range with 0.02°/step and 2 s/step.

The porous properties were determined via N_2 adsorption–desorption at -196°C using an automatic volumetric sorption analyzer (Autosorb-1 MP, Quantachrome, Boynton Beac, FL, USA). Before the measurements, the samples were outgassed at 250 °C for 19 h under 5×10^{-9} Torr vacuum. The total surface area was determined via the multipoint BET method, and the total pore volume was determined at $P/P_0 = 0.99$. Micropore surface areas and volumes were determined via the t-plot method, and the mesopore size distributions via the Barrett–Joyner–Halenda (BJH) method.

The determination of Brønsted and Lewis acid sites was performed via Fourier transform infrared (FT-IR) spectroscopy, combined with in situ adsorption of pyridine using a Nicolet 5700 FTIR spectrometer (PerkinElmer Corporation, Waltham, MA, USA) under a resolution of 4 cm^{-1} , with OMNIC software 9.2 and a specially designed heated, high-vacuum IR cell with CaF_2 windows. Before the measurements, all samples were ground in a mortar and pressed into self-supported wafers (15 mg/cm^2), which were in situ outgassed at 450 °C for 1 h under vacuum (10^{-6} mbar). A background spectrum was recorded at 150 °C. The adsorption of pyridine vapors was performed at 150 °C by adding pulses of pyridine for 1 h at a total cell pressure of 1 mbar. Afterwards, the spectra were recorded at 150 °C, after equilibration with pyridine at that temperature and after outgassing for 30 min at higher temperatures (250–450 °C) to evaluate the strength of the acid sites. Pyridinium ion bands at 1545 cm^{-1} and 1450 cm^{-1} (coordinated pyridine) were used to identify and quantify the Brønsted and Lewis acid sites, respectively.

X-ray photoelectron spectroscopy (XPS) was conducted using a Kratos Analytical AXIS UltraDLD system (Kratos Analytical Ltd., Manchester, UK) equipped with a monochromatic aluminum X-ray source (Al K α , 1486.6 eV). Measurements were performed under ultra-high vacuum conditions (10^{-9} Torr). Wide-scan spectra (full range) were recorded over

the entire binding energy range with a pass energy of 160 eV, utilizing an X-ray source power of 105 W. High-resolution (HR) regions were recorded with a pass energy of 20 eV, involving three to five sweeps in 0.1 eV steps and an X-ray source power of 150 W. To account for surface charging, the C 1s peak at 284.6 ± 0.2 eV (C-C bonds) was used as the reference. Surface cleaning was performed by Ar⁺ ion sputtering, with a nominal etch rate of ~ 100 Å/min for 72 s across a 4 mm² area. Spectral analysis included Shirley background subtraction. Peaks were fitted using a mixed Gaussian (70%) and Lorentzian (30%) model, with asymmetric adjustments for metallic nickel Ni⁰ peaks. Quantitative analysis employed relative sensitivity factors (RSFs) sourced from the Vision 2.2.10 software database.

Regarding the used catalysts, apart from the above-mentioned characterizations, elemental analysis was carried out to determine the carbon depositions. The analysis was performed in an elemental analyzer EA 3100 (EuroVector, Pavia, Italy). Furthermore, coke depositions were also determined via thermogravimetric analysis using an STA 449 F5 Jupiter instrument (Netzsch, Selb, Germany). The analysis was performed in the temperature range of 25–950 °C, under an air flow of 50 mL/min and a heating rate of 10 °C/min.

3.2. Catalytic Hydrodeoxygenation Experiments

3.2.1. Hydrodeoxygenation of Phenolic Compounds

The hydrodeoxygenation experiments with the model monomeric compounds (phenol, o-/m-cresol, catechol, anisole, guaiacol, syringol, creosol, 2-methoxy-4-methyl-phenol, and 1,2,3-trimethoxybenzene) and dimer (2-phenoxy-1-phenyl ethanol) were performed in a 50 mL stainless-steel, high-temperature/high-pressure batch autoclave reactor (Parr, Moline, IL, USA, model 4848) equipped with a magnetic stirrer. In each experiment, 0.2 g of the reactant was dissolved in 20 mL hexadecane (1% *w/v*), mixed with 0.04 g catalyst (catalyst-to-feed ratio, C/F = 0.2), and placed into the reactor. After flushing the reactor with H₂ three times to remove air, 50 bar H₂ was charged into the reactor, and the reaction was carried out at 220 °C for 60 min under 400 rpm stirring. These conditions were selected based on previous in-house studies.

3.2.2. Hydrodeoxygenation of Surrogate Mixture

The surrogate mixture simulating the light fraction of lignin pyrolysis bio-oils was composed of the following compounds: 2-methyl phenol (6.1 wt.%), 3-methyl phenol (6.1 wt.%), 2,4-dimethyl phenol (3.0 wt.%), 2-methoxy phenol (15.2 wt.%), 2,6-dimethoxy phenol (27.3 wt.%), 2-methoxy-4-methyl phenol (15.2 wt.%), 2-methoxy-4-propyl phenol (9.1 wt.%), 1,2,3-trimethoxy benzene (3.0 wt.%), catechol (3.0 wt.%), 3-methyl catechol (6.1 wt.%), and 4-methyl catechol (6.1 wt.%). The hydrodeoxygenation experiments with the surrogate mixture were performed in the same reactor using 1–10 g of the surrogate mixture dissolved in 10–20 mL hexadecane (5–50% *w/v*) and 0.2–2 g catalyst (C/F = 0.1–0.2). After flushing the reactor with H₂ three times to remove air, 50–70 bar H₂ was charged into the reactor, and the reaction was conducted in the temperature range of 220–320 °C for 60–180 min under 400–600 rpm stirring.

3.2.3. Product Separation and Analysis

After completion of the experiments, the reactor was rapidly cooled down to room temperature, and the gaseous products were collected in a vacuum bag and analyzed in a GC equipped with a TCD and FID (HP5890 Series II, Agilent Technologies, Santa Clara, CA, USA). Suitable calibration curves were used for the quantification of each gas. The liquid product was separated from the catalyst via filtration and analyzed via a gas chromatography–mass spectrometry instrument (Agilent 6890N-MSD 5973 GC-MS, Palo Alto, CA, USA) equipped with an MTX-5 column (Restek, Bellefonte, PA, USA, 30 m × 0.25 mm × 0.25 µm) to qualitatively identify the hydrodeoxygenation products,

while the most abundant cycloalkanes as well as the unconverted phenolic/aromatic compounds were quantitatively determined via gas chromatography using a Shimadzu Nexis GC-2030 instrument (Shimadzu Corp., Kyoto, Japan) equipped with a capillary Mega-101 column (30 m × 0.35 mm × 0.45 μm) and flame ionization detector (FID). A more detailed procedure is given in the Supplementary Material. Conversion, product yields, and selectivity were calculated via the following equations:

$$\text{Conversion (\%)} = \frac{\text{moles of compound in feed} - \text{moles of compound in product}}{\text{moles of compound in feed}} * 100\% \quad (1)$$

$$\text{Yield (\%)} = \frac{\text{moles of product}}{\text{moles of feed}} * 100\% \quad (2)$$

$$\text{Selectivity (\%)} = \frac{\text{moles of product}}{\text{converted moles of compound/feed}} * 100\% \quad (3)$$

The recovered used catalyst was washed several times with ethanol and dried at 80 °C for 6 h under vacuum. Selected spent catalysts were regenerated according to the following procedure. Firstly, the spent catalysts were calcined under air atmosphere at 500 °C for 3 h and 2 °C/min heating rate and then reduced to 450 °C, for 3 h under 50 mL/min H₂ flow.

4. Conclusions

The Ni/BEA catalyst exhibits appropriate composition, structural, textural, and metal–acid bifunctional characteristics suitable for the hydrogenation/hydrodeoxygenation of phenolic and aromatic compounds under mild reaction conditions. Almost all the compounds used as feedstocks were fully converted to C₆–C₈ alkyl-cycloalkanes with up to 81% yield, while the product composition and carbon number distribution were strongly affected by the side group of the reactant compound. The main advantages of the Ni/BEA catalyst are the preference for the cleavage of C_{AR}-OH and C_{AR}-OCH₃ bonds without affecting the C_{AR}-CH₃. Its performance was also less affected by steric hindrance due to the size/shape of the various phenolic reactants, compared to other zeolites (by comparing with data from the literature).

The hydrodeoxygenation of the phenolic/aromatic surrogate mixture simulating the light fraction of lignin fast-pyrolysis bio-oil led to 59–100% conversion to 9–68 wt.% alkyl-cycloalkanes with C₆–C₉ hydrocarbons, which could be utilized as drop-in blending components in gasoline and aviation fuels. Ni/BEA exhibited good catalytic activity under mild hydrodeoxygenation conditions and adequate stability, resulting in relatively low carbonaceous/coke depositions. Unavoidably, the textural characteristics of spent Ni/BEA are inferior to those of the fresh catalyst, but the regeneration treatment (calcination–reduction) can recover most of the catalyst properties, including the Ni-reduced state. Furthermore, by selecting appropriate (mainly lower temperature and longer time) reaction conditions, alteration of the micro/mesoporous characteristics is substantially suppressed. Brønsted zeolitic acidity is the most affected property and can be partially recovered by applying mild hydrodeoxygenation conditions. Finally, prior to considering upscaling of the process via increasing the content of lignin bio-oil in the feed mixture, internal and external mass-transfer phenomena and kinetics should be investigated in detail.

Supplementary Materials: The following supporting information can be downloaded at: <https://www.mdpi.com/article/10.3390/catal15010048/s1>, Figure S1: XRD and N₂ physisorption isotherm and BJH pore-size distribution of 10%Ni/BETA (12.5) catalyst; Figure S2: GC-MS analysis of the products obtained after the hydrodeoxygenation of hydroxy- and alkyl-substituted phenols at 220 °C, 1 h, 50 bar H₂, 10%Ni/BETA (12.5), C/F = 0.2; Figure S3: GC-MS analysis of the products obtained after the hydrodeoxygenation of alkoxyated substituted phenols/benzenes at 220 °C, 1 h, 50 bar H₂, 10% Ni/BETA (12.5), C/F = 0.2; Figure S4: Maximum diameters of phenolic/aromatic compounds; Figure S5: Effects of different reaction conditions on the gaseous products of surrogate mixture hydrodeoxygenation over 10%Ni/BETA (12.5); Figure S6: Thermogravimetric analysis of spent 10%Ni/BETA (12.5); Figure S7: Effects of different reaction conditions on H/C ratio determined via elemental analysis of spent 10%Ni/BETA (12.5); Figure S8: XPS spectra of fresh, used, and regenerated catalyst; Table S1: Effects of different reaction conditions on the characteristic temperatures and weight losses (TGA) of spent 10%Ni/BETA (12.5). Detailed analysis of liquid products.

Author Contributions: Conceptualization, A.G.M. and K.S.T.; methodology, A.G.M., F.F.Z., D.K. and S.A.K.; formal analysis, A.G.M., F.F.Z., D.K. and S.A.K.; investigation, A.G.M., F.F.Z., D.K. and S.A.K.; data curation, A.G.M., F.F.Z., D.K. and S.A.K.; writing—original draft preparation, A.G.M.; writing—review and editing, A.G.M. and K.S.T.; supervision, A.G.M. and K.S.T.; funding acquisition, K.S.T. All authors have read and agreed to the published version of the manuscript.

Funding: This project has received funding from the European Union’s Horizon 2020 research and innovation program under grant agreement No. 101007130.

Data Availability Statement: Data are contained within the article or Supplementary Material.

Conflicts of Interest: The authors declare no conflicts of interest.

References

1. European Union. Regulation (EU) 2023/2405 of the European Parliament and of the Council of 18 October 2023 on ensuring a level playing field for sustainable air transport (ReFuelEU Aviation). *Off. J. Eur. Union* **2023**. Available online: <http://data.europa.eu/eli/reg/2023/2405/oj> (accessed on 15 December 2024).
2. Song, M.J.; Zhang, X.H.; Chen, Y.B.; Zhang, Q.; Chen, L.A.; Liu, J.G.; Ma, L.L. Hydroprocessing of lipids: An effective production process for sustainable aviation fuel. *Energy* **2023**, *283*, 129107. [[CrossRef](#)]
3. Why, E.S.K.; Ong, H.C.; Lee, H.V.; Chen, W.H.; Asikin-Mijan, N.; Varman, M. Conversion of bio-jet fuel from palm kernel oil and its blending effect with jet A-1 fuel. *Energy Convers. Manag.* **2021**, *243*, 114311. [[CrossRef](#)]
4. Alkhoori, S.; Alareeqi, S.; Dabbawala, A.A.; Siakavelas, G.; Latsiou, A.; Anjum, D.H.; Harfouche, M.; Vasiliades, M.A.; Hinder, S.J.; Baker, M.A.; et al. Steering palm oil hydrodeoxygenation towards biofuel production: An experimental and theoretical approach to unveil periodic trends. *Mater. Today Chem.* **2024**, *40*, 102240. [[CrossRef](#)]
5. Kordouli, E.; Lycourghiotis, S.; Bourikas, K.; Lycourghiotis, A.; Kordulis, C. Renewable diesel synthesis by hydro-processing in green solvents. *Curr. Opin. Green Sustain. Chem.* **2024**, *48*, 100936. [[CrossRef](#)]
6. Wang, H.L.; Yang, B.; Zhang, Q.; Zhu, W.B. Catalytic routes for the conversion of lignocellulosic biomass to aviation fuel range hydrocarbons. *Renew. Sustain. Energy Rev.* **2020**, *120*, 109612. [[CrossRef](#)]
7. Wang, W.C.; Tao, L. Bio-jet fuel conversion technologies. *Renew. Sustain. Energy Rev.* **2016**, *53*, 801–822. [[CrossRef](#)]
8. Wang, T.J.; Li, K.; Liu, Q.Y.; Zhang, Q.; Qiu, S.B.; Long, J.X.; Chen, L.G.; Ma, L.L.; Zhang, Q. Aviation fuel synthesis by catalytic conversion of biomass hydrolysate in aqueous phase. *Appl. Energy* **2014**, *136*, 775–780. [[CrossRef](#)]
9. Huber, G.W.; Chheda, J.N.; Barrett, C.J.; Dumesic, J.A. Production of liquid alkanes by aqueous-phase processing of biomass-derived carbohydrates. *Science* **2005**, *308*, 1446–1450. [[CrossRef](#)]
10. Kunkes, E.L.; Simonetti, D.A.; West, R.M.; Serrano-Ruiz, J.C.; Gartner, C.A.; Dumesic, J.A. Catalytic conversion of biomass to monofunctional hydrocarbons and targeted liquid-fuel classes. *Science* **2008**, *322*, 417–421. [[CrossRef](#)]
11. Lebedeva, D.; Schick, L.W.; Cracco, D.; Sangsuwan, W.; Castiella-Ona, G.; Silva, D.O.; Marson, A.; Grape, E.S.; Inge, A.K.; Rossi, L.M.; et al. Sustainable aviation fuel from prehydrolysis liquors. *Green Chem.* **2024**, *26*, 7258–7267. [[CrossRef](#)]
12. Lazaridis, P.A.; Fotopoulos, A.P.; Karakoulia, S.A.; Triantafyllidis, K.S. Catalytic Fast Pyrolysis of Kraft Lignin With Conventional, Mesoporous and Nanosized ZSM-5 Zeolite for the Production of Alkyl-Phenols and Aromatics. *Front. Chem.* **2018**, *6*, 295. [[CrossRef](#)] [[PubMed](#)]
13. Charisteidis, I.; Lazaridis, P.; Fotopoulos, A.; Pachatouridou, E.; Matsakas, L.; Rova, U.; Christakopoulos, P.; Triantafyllidis, K. Catalytic Fast Pyrolysis of Lignin Isolated by Hybrid Organosolv—Steam Explosion Pretreatment of Hardwood and Softwood Biomass for the Production of Phenolics and Aromatics. *Catalysts* **2019**, *9*, 935. [[CrossRef](#)]
14. Margellou, A.G.; Lazaridis, P.A.; Charisteidis, I.D.; Nitsos, C.K.; Pappa, C.P.; Fotopoulos, A.P.; Van den Bosch, S.; Sels, B.F.; Triantafyllidis, K.S. Catalytic fast pyrolysis of beech wood lignin isolated by different biomass (pre)treatment processes: Organosolv, hydrothermal and enzymatic hydrolysis. *Appl. Catal. A-Gen.* **2021**, *623*, 118298. [[CrossRef](#)]
15. Soldatos, P.; Margellou, A.; Pappa, C.; Torofias, S.; Matsakas, L.; Rova, U.; Christakopoulos, P.; Triantafyllidis, K. Conversion of beechwood organosolv lignin via fast pyrolysis and in situ catalytic upgrading towards aromatic and phenolic-rich bio-oil. *Sustain. Chem. Environ.* **2024**, *6*, 100107. [[CrossRef](#)]
16. Kim, J.S. Production, separation and applications of phenolic-rich bio-oil—A review. *Bioresour. Technol.* **2015**, *178*, 90–98. [[CrossRef](#)] [[PubMed](#)]
17. Shen, Z.; Shi, C.; Liu, F.; Wang, W.; Ai, M.; Huang, Z.; Zhang, X.; Pan, L.; Zou, J.J. Advances in Heterogeneous Catalysts for Lignin Hydrogenolysis. *Adv. Sci.* **2024**, *11*, e2306693. [[CrossRef](#)] [[PubMed](#)]
18. Li, B.S.; Feng, B.X.; Wu, K.Y.; Yang, T.H. Hydrodeoxygenation of lignin derived bio-oil into aromatic hydrocarbons over Ni-Cu-Ru/HZSM-5 catalyst. *J. Fuel Chem. Technol.* **2023**, *51*, 358–365. [[CrossRef](#)]

19. Zhao, M.X.; Hu, J.; Lu, P.; Wu, S.L.; Liu, C.; Sun, Y.H. Efficient hydrodeoxygenation of lignin-derived bio-oil to hydrocarbon fuels over bifunctional RuCoW/NC catalysts. *Fuel* **2022**, *326*, 125020. [[CrossRef](#)]
20. Zormpa, F.F.; Margellou, A.G.; Karakoulia, S.A.; Delli, E.; Triantafyllidis, K.S. Hydrodeoxygenation of lignin bio-oil model compounds and surrogate mixtures over zeolite supported nickel catalysts. *Catal. Today* **2024**, *433*, 114654. [[CrossRef](#)]
21. Zerva, C.; Karakoulia, S.A.; Kalogiannis, K.G.; Margellou, A.; Iliopoulou, E.F.; Lappas, A.A.; Papayannakos, N.; Triantafyllidis, K.S. Hydrodeoxygenation of phenol and biomass fast pyrolysis oil (bio-oil) over Ni/WO₃-ZrO₂ catalyst. *Catal. Today* **2021**, *366*, 57–67. [[CrossRef](#)]
22. Mortensen, P.M.; Grunwaldt, J.D.; Jensen, P.A.; Jensen, A.D. Screening of Catalysts for Hydrodeoxygenation of Phenol as a Model Compound for Bio-oil. *ACS Catal.* **2013**, *3*, 1774–1785. [[CrossRef](#)]
23. Kim, H.; Lim, Y.H.; Park, J.H.; Ha, J.-M.; Kim, D.H. Hydrodeoxygenation of guaiacol over physically mixed Co/TiO₂ and WO₃/TiO₂ catalysts. *Green Chem.* **2024**, *26*, 2692–2704. [[CrossRef](#)]
24. Gracia, J.; Ayala-Cortés, A.; Di Stasi, C.; Remón, J.; Torres, D.; Pinilla, J.L.; Suelves, I. Highly selective catalytic hydrodeoxygenation of guaiacol to benzene in continuous operation mode. *Fuel Process. Technol.* **2024**, *255*, 108064. [[CrossRef](#)]
25. Zhang, W.; Chen, J.Z.; Liu, R.L.; Wang, S.P.; Chen, L.M.; Li, K.G. Hydrodeoxygenation of Lignin-Derived Phenolic Monomers and Dimers to Alkane Fuels over Bifunctional Zeolite-Supported Metal Catalysts. *ACS Sustain. Chem. Eng.* **2014**, *2*, 683–691. [[CrossRef](#)]
26. Sun, M.; Zhang, Y.; Liu, W.; Zhao, X.; Luo, H.; Miao, G.; Wang, Z.; Li, S.; Kong, L. Synergy of metallic Pt and oxygen vacancy sites in Pt-WO_{3-x} catalysts for efficiently promoting vanillin hydrodeoxygenation to methylcyclohexane. *Green Chem.* **2022**, *24*, 9489–9495. [[CrossRef](#)]
27. Sankaranarayanan, T.M.; Berenguer, A.; Ochoa-Hernández, C.; Moreno, I.; Jana, P.; Coronado, J.M.; Serrano, D.P.; Pizarro, P. Hydrodeoxygenation of anisole as bio-oil model compound over supported Ni and Co catalysts: Effect of metal and support properties. *Catal. Today* **2015**, *243*, 163–172. [[CrossRef](#)]
28. Mohammed, A.A.; Tannous, J.H. Catalytic Hydrodeoxygenation of Phenols and Cresols to Gasoline Range Biofuels. *Chem. Rec.* **2024**, *24*, e202400092. [[CrossRef](#)]
29. Zhang, X.; Yan, H.; Zhu, L.J.; Li, T.; Wang, S.R. Hydrodeoxygenation of Lignin-Derived Monomers and Dimers over a Ru Supported Solid Super Acid Catalyst for Cycloalkane Production. *Adv. Sustain. Syst.* **2020**, *4*, 1900136. [[CrossRef](#)]
30. Yan, B.; Ding, W.; Shi, G.; Lin, X.; Zhang, S. Study on the catalytic hydrodeoxygenation of lignin dimers: Adsorption properties and linkages cleavage. *Bioresour. Technol.* **2024**, *394*, 130264. [[CrossRef](#)] [[PubMed](#)]
31. Zhao, C.; Lercher, J.A. Selective Hydrodeoxygenation of Lignin-Derived Phenolic Monomers and Dimers to Cycloalkanes on Pd/C and HZSM-5 Catalysts. *Chemcatchem* **2012**, *4*, 64–68. [[CrossRef](#)]
32. Zhang, X.; Zhang, Q.; Wang, T.; Ma, L.; Yu, Y.; Chen, L. Hydrodeoxygenation of lignin-derived phenolic compounds to hydrocarbons over Ni/SiO₂-ZrO₂ catalysts. *Bioresour. Technol.* **2013**, *134*, 73–80. [[CrossRef](#)] [[PubMed](#)]
33. Shafaghat, H.; Rezaei, P.S.; Daud, W.M.A.W. Catalytic hydrodeoxygenation of simulated phenolic bio-oil to cycloalkanes and aromatic hydrocarbons over bifunctional metal/acid catalysts of Ni/HBeta, Fe/HBeta and NiFe/HBeta. *J. Ind. Eng. Chem.* **2016**, *35*, 268–276. [[CrossRef](#)]
34. Yao, G.; Wu, G.J.; Dai, W.L.; Guan, N.J.; Li, L.D. Hydrodeoxygenation of lignin-derived phenolic compounds over bi-functional Ru/H-Beta under mild conditions. *Fuel* **2015**, *150*, 175–183. [[CrossRef](#)]
35. Dimitriadis, A.; Chrysikou, L.P.; Meletidis, G.; Terzis, G.; Auersvald, M.; Kubicka, D.; Bezergianni, S. Bio-based refinery intermediate production via hydrodeoxygenation of fast pyrolysis bio-oil. *Renew. Energy* **2021**, *168*, 593–605. [[CrossRef](#)]
36. Kumar, A.; Khani, Y.; Ko, C.H.; Jae, J.; Banerjee, A.; Bhaskar, T.; Park, Y.-K. Production of Valuable Aromatics from the Hydrodeoxygenation of Guaiacol and Real Bio-Oil over Ni-Nb/HZSM-5 under Supercritical Ethanol. *ACS Sustain. Chem. Eng.* **2024**, *12*, 10786–10804. [[CrossRef](#)]
37. Duan, H.; Dong, J.; Gu, X.; Peng, Y.K.; Chen, W.; Issariyakul, T.; Myers, W.K.; Li, M.J.; Yi, N.; Kilpatrick, A.F.R.; et al. Hydrodeoxygenation of water-insoluble bio-oil to alkanes using a highly dispersed Pd-Mo catalyst. *Nat. Commun.* **2017**, *8*, 591. [[CrossRef](#)]
38. Templis, C.C.; Revelas, C.J.; Papastilianou, A.A.; Papayannakos, N.G. Phenol Hydrodeoxygenation over a Reduced and Sulfided NiMo/ γ -Al₂O₃ Catalyst. *Ind. Eng. Chem. Res.* **2019**, *58*, 6278–6287. [[CrossRef](#)]
39. Kristensen, T.A.; Hultberg, C.P.; Wallenberg, R.L.; Abdelaziz, O.Y.; Blomberg, S. Promoting Effect of Ce and La on Ni-Mo/ δ -Al₂O₃ Catalysts in the Hydrodeoxygenation of Vanillin. *Energy Fuels* **2024**, *38*, 9827–9835. [[CrossRef](#)] [[PubMed](#)]
40. Li, X.; Chen, G.; Liu, C.; Ma, W.; Yan, B.; Zhang, J. Hydrodeoxygenation of lignin-derived bio-oil using molecular sieves supported metal catalysts: A critical review. *Renew. Sustain. Energy Rev.* **2017**, *71*, 296–308. [[CrossRef](#)]
41. Viljava, T.R.; Komulainen, R.S.; Krause, A.O.I. Effect of H₂S on the stability of CoMo/Al₂O₃ catalysts during hydrodeoxygenation. *Catal. Today* **2000**, *60*, 83–92. [[CrossRef](#)]
42. Robinson, A.M.; Hensley, J.E.; Medlin, J.W. Bifunctional Catalysts for Upgrading of Biomass-Derived Oxygenates: A Review. *ACS Catal.* **2016**, *6*, 5026–5043. [[CrossRef](#)]

43. Gollakota, A.R.K.; Shu, C.-M.; Sarangi, P.K.; Shadangi, K.P.; Rakshit, S.; Kennedy, J.F.; Gupta, V.K.; Sharma, M. Catalytic hydrodeoxygenation of bio-oil and model compounds—Choice of catalysts, and mechanisms. *Renew. Sustain. Energy Rev.* **2023**, *187*, 113700. [CrossRef]
44. Yang, Y.; Xu, X.; He, H.; Huo, D.; Li, X.; Dai, L.; Si, C. The catalytic hydrodeoxygenation of bio-oil for upgradation from lignocellulosic biomass. *Int. J. Biol. Macromol.* **2023**, *242*, 124773. [CrossRef] [PubMed]
45. Ambursa, M.M.; Juan, J.C.; Yahaya, Y.; Taufiq-Yap, Y.H.; Lin, Y.-C.; Lee, H.V. A review on catalytic hydrodeoxygenation of lignin to transportation fuels by using nickel-based catalysts. *Renew. Sustain. Energy Rev.* **2021**, *138*, 110667. [CrossRef]
46. de Souza, P.M.; Rabelo-Neto, R.C.; Borges, L.E.P.; Jacobs, G.; Davis, B.H.; Resasco, D.E.; Noronha, F.B. Hydrodeoxygenation of Phenol over Pd Catalysts. Effect of Support on Reaction Mechanism and Catalyst Deactivation. *ACS Catal.* **2017**, *7*, 2058–2073. [CrossRef]
47. Ghampson, I.T.; Sepúlveda, C.; Dongil, A.B.; Pecchi, G.; García, R.; Fierro, J.L.G.; Escalona, N. Phenol hydrodeoxygenation: Effect of support and Re promoter on the reactivity of Co catalysts. *Catal. Sci. Technol.* **2016**, *6*, 7289–7306. [CrossRef]
48. Teles, C.A.; de Souza, P.M.; Rabelo-Neto, R.C.; Teran, A.; Jacobs, G.; Vilela Weikert, C.; Magriotis, Z.M.; Gonçalves, V.O.O.; Resasco, D.E.; Noronha, F.B. Reaction pathways for the HDO of guaiacol over supported Pd catalysts: Effect of support type in the deoxygenation of hydroxyl and methoxy groups. *Mol. Catal.* **2022**, *523*, 111491. [CrossRef]
49. Yan, P.; Bryant, G.; Li, M.M.-J.; Mensah, J.; Kennedy, E.; Stockenhuber, M. Shape selectivity of zeolite catalysts for the hydrodeoxygenation of biocrude oil and its model compounds. *Microporous Mesoporous Mater.* **2020**, *309*, 110561. [CrossRef]
50. Song, W.; Liu, Y.; Baráth, E.; Zhao, C.; Lercher, J.A. Synergistic effects of Ni and acid sites for hydrogenation and C–O bond cleavage of substituted phenols. *Green Chem.* **2015**, *17*, 1204–1218. [CrossRef]
51. Park, J.H.; Kim, H.; Jung, H.; Ha, J.-M.; Kim, D.H. Investigation of ruthenium loaded beta zeolite catalyst performance in vanillin hydrodeoxygenation yielding both monomeric and dimeric cycloalkanes. *Chem. Eng. J.* **2024**, *499*, 155888. [CrossRef]
52. Kumar, A.; Kumar, A.; Santosa, D.M.; Wang, H.; Zuo, P.; Wang, C.; Mittal, A.; Gieleciak, R.; Klein, D.P.; Manto, M.J.; et al. Engineered Ru on HY zeolite catalyst for continuous and selective hydrodeoxygenation of lignin phenolics to cycloalkanes under moderate conditions. *Appl. Catal. A Gen.* **2024**, *676*, 119649. [CrossRef]
53. Shafaghat, H.; Sirous Rezaei, P.; Daud, W.M.A.W. Catalytic hydrogenation of phenol, cresol and guaiacol over physically mixed catalysts of Pd/C and zeolite solid acids. *RSC Adv.* **2015**, *5*, 33990–33998. [CrossRef]
54. Yan, P.; Li, M.M.-J.; Kennedy, E.; Adesina, A.; Zhao, G.; Setiawan, A.; Stockenhuber, M. The role of acid and metal sites in hydrodeoxygenation of guaiacol over Ni/Beta catalysts. *Catal. Sci. Technol.* **2020**, *10*, 810–825. [CrossRef]
55. Thommes, M.; Kaneko, K.; Neimark, A.V.; Olivier, J.P.; Rodriguez-Reinoso, F.; Rouquerol, J.; Sing, K.S.W. Physisorption of gases, with special reference to the evaluation of surface area and pore size distribution (IUPAC Technical Report). *Pure Appl. Chem.* **2015**, *87*, 1051–1069. [CrossRef]
56. Yu, Z.; Wang, A.; Liu, S.; Yao, Y.; Sun, Z.; Li, X.; Liu, Y.; Wang, Y.; Camaioni, D.M.; Lercher, J.A. Hydrodeoxygenation of phenolic compounds to cycloalkanes over supported nickel phosphides. *Catal. Today* **2019**, *319*, 48–56. [CrossRef]
57. López, M.; Palacio, R.; Mamede, A.-S.; Fernández, J.J.; Royer, S. Hydrodeoxygenation of guaiacol into cyclohexane over mesoporous silica supported Ni–ZrO₂ catalyst. *Microporous Mesoporous Mater.* **2020**, *309*, 110452. [CrossRef]
58. Lin, Y.-C.; Li, C.-L.; Wan, H.-P.; Lee, H.-T.; Liu, C.-F. Catalytic Hydrodeoxygenation of Guaiacol on Rh-Based and Sulfided CoMo and NiMo Catalysts. *Energy Fuels* **2011**, *25*, 890–896. [CrossRef]
59. Available online: <https://www.iza-structure.org/> (accessed on 13 December 2024).
60. Jmol: An Open-Source Java Viewer for Chemical Structures in 3D. Available online: <http://www.jmol.org/> (accessed on 25 November 2024).
61. Jae, J.; Tompsett, G.A.; Foster, A.J.; Hammond, K.D.; Auerbach, S.M.; Lobo, R.F.; Huber, G.W. Investigation into the shape selectivity of zeolite catalysts for biomass conversion. *J. Catal.* **2011**, *279*, 257–268. [CrossRef]
62. Yan, P.; Kennedy, E.; Stockenhuber, M. Natural zeolite supported Ni catalysts for hydrodeoxygenation of anisole. *Green Chem.* **2021**, *23*, 4673–4684. [CrossRef]
63. Zhu, X.; Lobban, L.L.; Mallinson, R.G.; Resasco, D.E. Bifunctional transalkylation and hydrodeoxygenation of anisole over a Pt/HBeta catalyst. *J. Catal.* **2011**, *281*, 21–29. [CrossRef]
64. Ghampson, I.T.; Canales, R.; Escalona, N. A study of the hydrodeoxygenation of anisole over Re–MoO_x/TiO₂ catalyst. *Appl. Catal. A Gen.* **2018**, *549*, 225–236. [CrossRef]
65. Güvenatam, B.; Kurşun, O.; Heeres, E.H.J.; Pidko, E.A.; Hensen, E.J.M. Hydrodeoxygenation of mono- and dimeric lignin model compounds on noble metal catalysts. *Catal. Today* **2014**, *233*, 83–91. [CrossRef]
66. Li, L.; Huang, Z.; Shu, F.; Gao, Y.; Long, J. Hydrodeoxygenation of heavy lignin bio-oil to oxygenated fuel catalyzed by Cu_xNi_y/MgO. *Fuel* **2024**, *357*, 129805. [CrossRef]
67. Fu, Z.-P.; Zhao, Y.-P.; Wu, F.-P.; Xie, J.-X.; Qiu, L.-L.; Xiao, J.; Liang, J.; Bai, Y.-H.; Liu, F.-J.; Cao, J.-P. Selective hydrogenolysis of C–O bonds in lignin model compounds and Kraft lignin over highly efficient Ni_xCo_yAl catalysts. *Mol. Catal.* **2023**, *547*, 113334. [CrossRef]

68. Le, T.M.; Pham, X.-T.; Ho, P.H.; Pham, T.L.M.; Cao, X.T.; Nguyen, T.N.; Giang, H.N.; Phung, T.K. Catalytic Conversion of 2-Phenethyl Phenyl Ether and 2-Phenoxy-1-Phenyl Ethanol Over ZSM-5, Y and Beta Zeolites. *ChemistrySelect* **2024**, *9*, e202403967. [[CrossRef](#)]
69. Jastrzebski, R.; Constant, S.; Lancefield, C.S.; Westwood, N.J.; Weckhuysen, B.M.; Bruijninx, P.C.A. Tandem Catalytic Depolymerization of Lignin by Water-Tolerant Lewis Acids and Rhodium Complexes. *ChemSusChem* **2016**, *9*, 2074–2079. [[CrossRef](#)] [[PubMed](#)]
70. Zhang, J.; Tian, F.; Chen, J.; Shi, Y.; Cao, H.; Ning, P.; Sun, S.; Xie, Y. Conversion of phenol to cyclohexane in the aqueous phase over Ni/zeolite bi-functional catalysts. *Front. Chem. Sci. Eng.* **2021**, *15*, 288–298. [[CrossRef](#)]
71. Wang, Y.; Huang, H.; Baxter, N.C.; Liao, Y.; Zhao, Y.; Wang, S. Guaiacol hydrodeoxygenation over Pd catalyst with mesoporous ZSM-5 support synthesized by solid-state crystallization. *Catal. Today* **2020**, *358*, 60–67. [[CrossRef](#)]
72. Hafeez, S.; Aristodemou, E.; Manos, G.; Al-Salem, S.M.; Constantinou, A. Computational fluid dynamics (CFD) and reaction modelling study of bio-oil catalytic hydrodeoxygenation in microreactors. *React. Chem. Eng.* **2020**, *5*, 1083–1092. [[CrossRef](#)]
73. Subramanyam, M.D.; Gollakota, A.R.K.; Kishore, N. CFD simulations of catalytic hydrodeoxygenation of bio-oil using Pt/Al₂O₃ in a fixed bed reactor. *RSC Adv.* **2015**, *5*, 90354–90366. [[CrossRef](#)]
74. Gollakota, A.R.K.; Subramanyam, M.D.; Kishore, N.; Gu, S. CFD simulations on the effect of catalysts on the hydrodeoxygenation of bio-oil. *RSC Adv.* **2015**, *5*, 41855–41866. [[CrossRef](#)]
75. Li, Y.; Zhang, C.; Liu, Y.; Tang, S.; Chen, G.; Zhang, R.; Tang, X. Coke formation on the surface of Ni/HZSM-5 and Ni-Cu/HZSM-5 catalysts during bio-oil hydrodeoxygenation. *Fuel* **2017**, *189*, 23–31. [[CrossRef](#)]
76. Anekwe, I.M.S.; Chetty, M.; Khotseng, L.; Kiambi, S.L.; Maharaj, L.; Oboirien, B.; Isa, Y.M. Stability, deactivation and regeneration study of a newly developed HZSM-5 and Ni-doped HZSM-5 zeolite catalysts for ethanol-to-hydrocarbon conversion. *Catal. Commun.* **2024**, *186*, 106802. [[CrossRef](#)]
77. Vogt, E.T.C.; Fu, D.; Weckhuysen, B.M. Carbon Deposit Analysis in Catalyst Deactivation, Regeneration, and Rejuvenation. *Angew. Chem. Int. Ed. Engl.* **2023**, *62*, e202300319. [[CrossRef](#)]
78. Biesinger, M.C.; Payne, B.P.; Lau, L.W.M.; Gerson, A.; Smart, R.S.C. X-ray photoelectron spectroscopic chemical state quantification of mixed nickel metal, oxide and hydroxide systems. *Surf. Interface Anal.* **2009**, *41*, 324–332. [[CrossRef](#)]
79. Jiang, Y.; Chen, J.; Zhang, J.; Zeng, Y.; Wang, Y.; Zhou, F.; Kiani, M.; Wang, R. Controlled decoration of Pd on Ni(OH)₂ nanoparticles by atomic layer deposition for high ethanol oxidation activity. *Appl. Surf. Sci.* **2017**, *420*, 214–221. [[CrossRef](#)]
80. Gardner, T.H.; Shekhawat, D.; Berry, D.A.; Smith, M.W.; Salazar, M.; Kugler, E.L. Effect of nickel hexaaluminate mirror cation on structure-sensitive reactions during n-tetradecane partial oxidation. *Appl. Catal. A Gen.* **2007**, *323*, 1–8. [[CrossRef](#)]
81. Komvokis, V.G.; Karakoulia, S.; Iliopoulou, E.F.; Papapetrou, M.C.; Vasalos, I.A.; Lappas, A.A.; Triantafyllidis, K.S. Upgrading of Fischer–Tropsch synthesis bio-waxes via catalytic cracking: Effect of acidity, porosity and metal modification of zeolitic and mesoporous aluminosilicate catalysts. *Catal. Today* **2012**, *196*, 42–55. [[CrossRef](#)]
82. Triantafyllidis, K.S.; Nalbandian, L.; Trikalitis, P.N.; Ladavos, A.K.; Mavromoustakos, T.; Nicolaidis, C.P. Structural, compositional and acidic characteristics of nanosized amorphous or partially crystalline ZSM-5 zeolite-based materials. *Microporous Mesoporous Mater.* **2004**, *75*, 89–100. [[CrossRef](#)]
83. Triantafyllidis, C.S.; Vlessidis, A.G.; Nalbandian, L.; Evmiridis, N.P. Effect of the degree and type of the dealumination method on the structural, compositional and acidic characteristics of H-ZSM-5 zeolites. *Microporous Mesoporous Mater.* **2001**, *47*, 369–388. [[CrossRef](#)]
84. Triantafyllidis, C.S.; Vlessidis, A.G.; Evmiridis, N.P. Dealuminated H–Y Zeolites: Influence of the Degree and the Type of Dealumination Method on the Structural and Acidic Characteristics of H–Y Zeolites. *Ind. Eng. Chem. Res.* **2000**, *39*, 307–319. [[CrossRef](#)]
85. Zhao, C.; Kasakov, S.; He, J.; Lercher, J.A. Comparison of kinetics, activity and stability of Ni/HZSM-5 and Ni/Al₂O₃-HZSM-5 for phenol hydrodeoxygenation. *J. Catal.* **2012**, *296*, 12–23. [[CrossRef](#)]
86. Cordero-Lanzac, T.; Palos, R.; Hita, I.; Arandes, J.M.; Rodríguez-Mirasol, J.; Cordero, T.; Bilbao, J.; Castaño, P. Revealing the pathways of catalyst deactivation by coke during the hydrodeoxygenation of raw bio-oil. *Appl. Catal. B Environ.* **2018**, *239*, 513–524. [[CrossRef](#)]

Disclaimer/Publisher’s Note: The statements, opinions and data contained in all publications are solely those of the individual author(s) and contributor(s) and not of MDPI and/or the editor(s). MDPI and/or the editor(s) disclaim responsibility for any injury to people or property resulting from any ideas, methods, instructions or products referred to in the content.